



TURBOMACHINERY & PUMP SYMPOSIA | HOUSTON, TX
SEPTEMBER 16-18, 2025
SHORT COURSES: SEPTEMBER 15, 2025

SEALED ENDS SQUEEZE FILM DAMPERS AND INTEGRAL SQUEEZE FILM DAMPERS ENGINEERING MODELS & EXPERIMENTAL VERIFICATION

Luis San Andrés,

Professor Emeritus

Lsanandres@tamu.edu

Texas A&M University, College Station, TX 77843, USA



Luis San Andrés performed research in lubrication and rotordynamics and produced advanced hydrostatic bearings for cryogenic turbo pumps, squeeze film dampers for aircraft jet engines, and gas foil bearings for oil-free micro turbomachinery. Luis was a Mechanical Engineer Professor at Texas A&M University (1991-2023) and a Principal Investigator of the Turbomachinery Laboratory (1985-2023). Luis is a Life Fellow of ASME, STLE and GPPS. Dr. San Andrés ASME honors include the 2022 Aircraft Engine Technology Award (International Gas Turbine Institute), the 2023 Mayo D. Hersey Award (Tribology Div.), and the 2025 Henry R. Worthington Medal (Fluids Engineering Div.). The tutorial sums the outcome of 36+ years of SFD experimental research, computational physics modeling, and engineering design conducted by graduate students of the Turbomachinery Laboratory of Texas A&M University. Visit URL <http://rotorlab.tamu.edu> for resources on vibrations, rotordynamics and lubrication of bearings, dampers, and seals.

ABSTRACT

Squeeze Film Dampers (SFDs) are effective means to ameliorate rotor vibration amplitudes and to suppress instabilities in rotor-bearing systems. A SFD is not an off-the-shelf mechanical element but tailored to a particular rotor-bearing system as its design must satisfy a desired damping ratio; if too low, the damper is ineffective, whereas if damping is too large, the SFD may lock thus aggravating the system response. In many cases, SFDs are also employed to control the placement of (rigid body) critical speeds and displacing the machine operation into a speed range ensuring an effective structural isolation.

Industry demands well-engineered SFDs with a low footprint to reduce cost, maintenance, weight, and space while pushing for higher operating shaft speeds to increase power output. Modern turbomachinery implements ultra-short length SFDs ($L/D \leq 0.2$) to satisfy stringent weight and space demands with a low parts count. SFDs with sealed ends, either O-rings or piston rings or end gap plates, are customarily used to amplify the viscous damping in a short length element. Simultaneously, added mass coefficients also increase. At large squeeze film velocities, air ingestion is persistent and produces a bubbly lubricant film with much less damping.

The tutorial reviews experimental results vis a vis model prediction for damping and inertia force coefficients of SFD configurations with end seals and operating over a wide range of conditions. The applications encompass gas and steam turbines, multiple stage pumps, and centrifugal compressors. Recent knowledge on the force coefficients for Integral Squeeze Film Dampers (ISFDs) with sealed end is also reviewed.

OUTCOMES or LEARNING OBJECTIVES

The tutorial reviews how SFDs generate viscous dissipation forces and fluid inertia forces aiding to reduce rotor vibrations. The knowledge extends to describe modern predictive tools vis a vis test data, a discussion on pervasive air ingestion at high squeeze film velocities v_s (= amplitude or motion \times whirl frequency), and knowledge on the effective selection of end seals to increase

viscous damping. The tutorial presents comparisons of experimentally identified damping (C) and inertia or added mass (M) coefficients versus amplitude of motion (orbit size) and static eccentricity position, both ranging from small to large, and over a range of whirl frequencies. Pressing questions on the design and operation of SFDs are answered, including:

- (a) When and where is damping needed? Is a lot of damping best?
- (b) How come SFDs do not have a stiffness or a static centering ability?
- (c) Why do SFDs produce a sizeable added mass or virtual mass?
- (d) How much more damping is available from a damper with end seals? Are piston rings better than O-rings? Which type to select?
- (e) How many feed holes does a damper require? What about if a feed hole plugs?
- (f) Does the amplitude and shape of whirl motion affect the SFD force coefficients?
- (g) Is air ingestion a persistent issue with SFDs having sealed ends, piston rings in particular?
- (h) How to quantify the amount of gas ingested in actual SFD operation.
- (i) Do ISFDs produce just damping? Why do manufacturers ignore the obvious? How does the gap from end seals affect the ISFD damping coefficients?
- (j) How do predictions from modern SFD models correlate with the experimental record? Do small amplitude journal motions produce the same damping coefficient as large amplitude whirl motions do? Which one is important?

BACKGROUND

Squeeze film bearing dampers (SFDs) are lubricated elements providing viscous damping in mechanical systems. Squeeze film dampers in rotating machinery provide structural isolation, reduce the amplitudes of rotor response to imbalance, and in some instances, assist to suppress rotordynamic instability.

The most commonly recurring problems in rotordynamics are excessive steady state synchronous vibration levels and subsynchronous rotor instabilities. The first problem may be reduced by improved balancing, or by introducing modifications into the rotor-bearing system to move the system critical speeds out of the operating range, or by introducing external damping to limit peak amplitudes at traversed critical speeds. Subsynchronous rotor instabilities may be avoided by eliminating the instability mechanism, by rising the natural frequency of the rotor-bearing system as high as possible, or by introducing damping to increase the onset rotor speed of instability [1,2].

Lightweight, high-performance engines exhibit a trend towards increased flexibility leading to a high sensitivity to imbalance with large vibration levels and reduced reliability. Squeeze film dampers (SFDs) are essential components of high-speed turbomachinery since they offer the unique advantages of dissipation of vibration energy and isolation of structural components, as well as the capability to improve the dynamic stability characteristics of inherently unstable rotor-bearing systems. SFDs are used primarily in aircraft jet engines to provide viscous damping to rolling element bearings which themselves have little or no damping. One other important application is related to high performance compressor units where SFDs are installed in series with tilting pad bearings to reduce (soften) bearing support stiffness while providing additional damping as a safety mechanism to prevent rotordynamic instabilities. In addition, in geared compressors, a SFD assists to reduce and isolate multiple frequency excitations transmitted through the bull gear, for example.

Where is damping needed? Is a lot of damping best?

Figure 1 depicts a single degree of freedom (SDOF) mechanical system comprising a mass (M_e) supported by a linear spring with stiffness (K_e) and a dashpot with (viscous) damping coefficient (C_e). The mass and spring are conservative mechanical elements that store kinetic and potential strain energy, respectively, whereas the dashpot dissipates mechanical energy. The system

natural frequency equals $f_n = 2\pi \omega_n = 2\pi \sqrt{K_e/M_e}$ (Hz), and the system damping ratio is $\zeta = C/C_{crit}$, where

$C_{crit} = 2\sqrt{K_e M_e} = 2K_e/\omega_n = 2M_e \omega_n$ is a critical damping coefficient. In a rotating mechanical system, (M_e, K_e) may represent the

rotor modal mass and bending stiffness, for example; or with a rigid rotor, the rotating mass and the (bearing) support stiffness. The graphs on the right depict the amplitude of response of the system due to a periodic force induced by mass imbalance with magnitude (u) and frequency (ω) that coincides with the rotor spinning angular speed. Note the amplitude of response $|X/u|$ peaks at a whirl frequency near the natural frequency (f_n). This frequency is known as a critical speed. Similarly, the transmitted force to

ground peaks near f_n . The larger the damping ratio (ζ), the lower the amplitude of system motion as well as the transmitted force. At the critical speed, for small $\zeta < 0.2$, the peak amplitude $|X/u|_{\max} = A = 1/(2\zeta)$ is known as the system amplification factor. Note that although damping is needed over a narrow region of whirl frequencies, only damping allows a (rotor-bearing) system to traverse its critical speed. In addition, damping also increases force transmissibility for operation with whirl frequencies $> \sqrt{2} f_n$.

From the results shown one realizes that the physical magnitude of the damping coefficient (C_e) has meaning only when compared to the system critical damping coefficient (C_{crit}), a property of the mechanical system. That is, the damping ratio (ζ) is the important design variable, and not the magnitude of C_e . This is the reason why SFDs are not off the shelf elements. A damper must be tailored to the physical system.

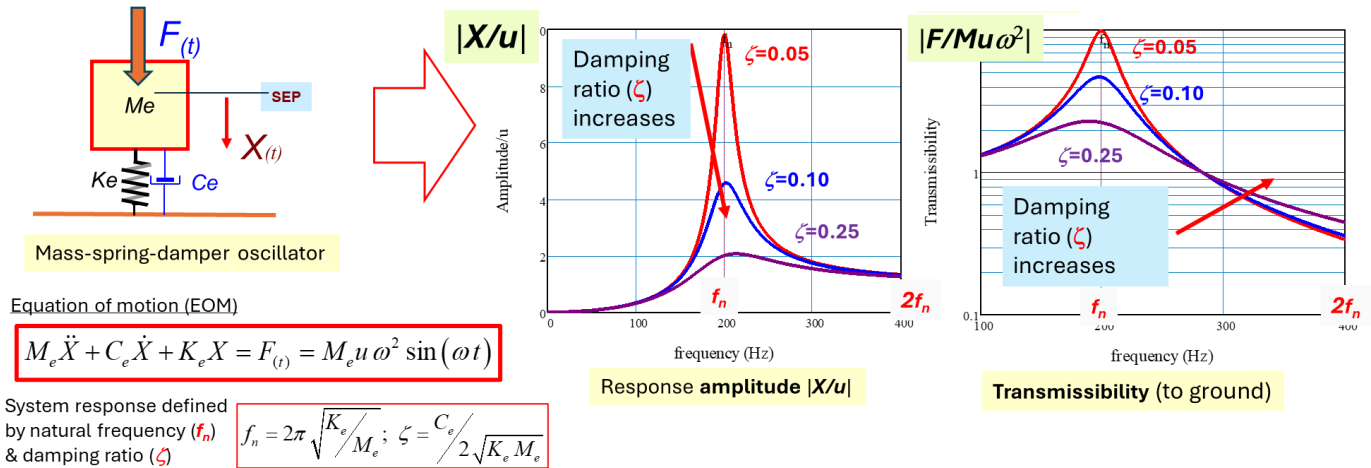


Fig. 1 The simplest $(K,C,M)_e$ mechanical system and the amplitude of response and force transmissibility due to a periodic force induced by imbalance.

Advancing to a more realistic system, Figure 2 depicts a two-DOF mechanical system representing a simple rotor $(K,C,M)_e$ supported on a flexible damped support with stiffness K_S and mass M_S . The coefficient C_{SFD} represents an idealized squeeze film damper. The system is tuned to $(K_S/M_S) = 0.1 (K_e/M_e) = 1/10 f_n^2$. The two-DOF system has two natural frequencies, f_{n1} and f_{n2} , below and above the original natural frequency (f_n). The graphs on the right show the amplitude of response $|X/u|$ and the transmitted force ratio vs. whirl frequency (= rotor speed). Note that, while traversing a natural frequency, both the amplitude of response and the force transmissibility ratio decrease as the damping ratio (ζ) increases. However, too much damping ($\zeta=0.2$) locks the support and worsens the system response in a frequency range enclosing the original natural frequency (f_n). That is, too much damping prevents the support to move.

To close this section, every rotor-bearing system could be designed to operate with an optimum damping coefficient, a function of a stiffness ratio (damper support K /rotor bending K). As a practitioner do keep handy the seminal work of Barrett et al. [3] (1978) that publishes the equations for the selection of physical parameters that make an optimum flexibly damped support. Incidentally, the proper selection of the support stiffness (K_S) allows for an engineered placement of system critical speeds away from the mean operating rotor speed. Extending a prior statement, the SFD and its support stiffness must be tailored to the rotor-bearing system to control the placement of critical speeds and to reduce amplitude of whirl motions, while also increasing the stability of a rotor-bearing system.

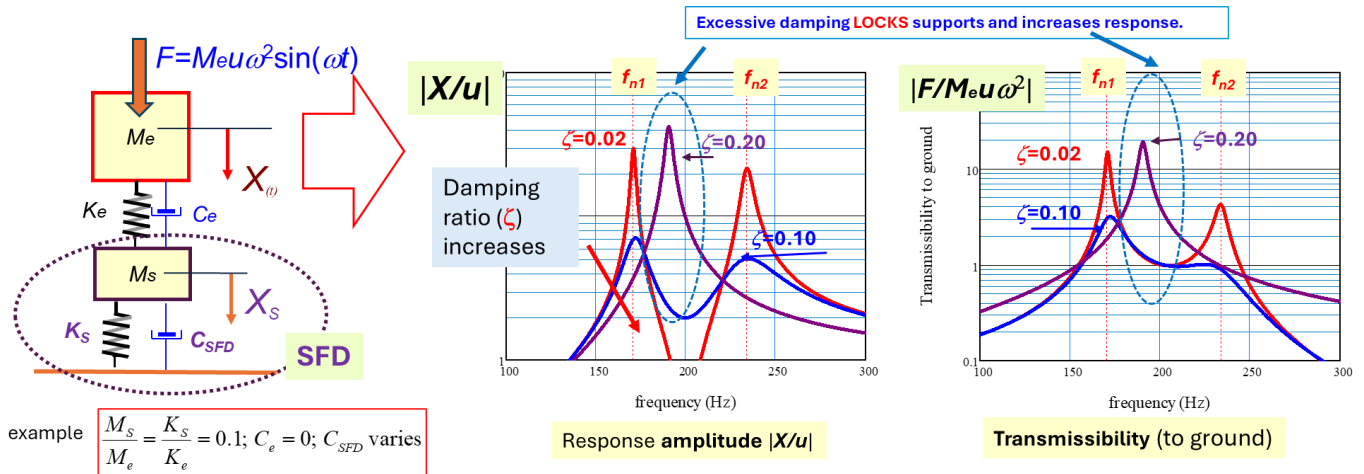


Fig. 2 A two-DOF simple mechanical system. Effect of damping from a flexible support on the amplitude of response and force transmissibility due to a periodic force.

FUNDAMENTALS OF THE APPLICATION

Since 1975 the TAMU Turbomachinery Symposium (TPS) has showcased numerous lectures detailing applications of SFDs to rotating machinery, in particular compressors and steam turbines. For a concise review of the publications appearing at the Symposium, please read Refs. [1,2] or access the papers directly at <http://turbolab.tamu.edu/proc/>. A few references of importance to this tutorial follow.

Zeidan et al. [4] (1996) review the history of SFDs in jet engines and detail design practices for ready SFD implementation in commercial oil and gas centrifugal compressors. In the same year, Kuzdal and Hustak [5] present experimental results for the synchronous (imbalance) response of a rotor supported in various damper types, centered and off centered, some installed with O-rings as end seals. The authors found that centered dampers offer better control of rotor amplitudes of motion than off-centered (eccentric) dampers do. In general, the recorded amplitudes of rotor motion while traversing its critical speed show more damping than analytical predictions based on classical lubrication theory. From the test results, the rotor-bearing system amplification ratio is smaller than analytical predictions otherwise indicate.

Despite the many successful applications, industry often recognizes that the design of SFDs is based on overly simplified predictive models that either fail to incorporate or simply neglect unique features (structural and fluidic) that affect a damper dynamic force performance. Actual damper performance can range from erratic to non-functioning depending on the operating conditions. San Andrés et al., significant advances on SFD experimentation, identification of force coefficients, and modern physical models for aircraft engines applications; see Refs. [6,7] (2016), [8] (2020), and [9] (2023).

Figure 3 shows a typical SFD configuration consisting of an inner nonrotating journal and a stationary outer bearing, both nearly equal in diameter. The journal is mounted on the external race of a rolling element bearing and prevented from spinning with loose pins or a squirrel cage that provides a centering elastic mechanism. Between the journal and housing, the annular squeeze film, with a radial clearance equaling to a minute fraction of the journal diameter, is filled with a lubricant provided as a splash from the rolling element bearing lubrication system or by a dedicated pressurized delivery system. In operation, as the journal moves due to dynamic forces acting on the system, the fluid is displaced to accommodate these motions. As a result, hydrodynamic squeeze film pressures exert reaction forces on the journal and provide for a mechanism to attenuate transmitted forces and to reduce the rotor amplitude of motion.

In practice SFDs operate with a low oil feed pressure, max. 5 bar (73.5 psi), that generally does not prevent the lubricant in the fluid film lands from liquid vaporization or entrainment of external gaseous media into the film lands. Open ends SFDs or ends sealed SFDs (piston rings and end plate seals) are prone to develop a flow regime where the ingestion and entrainment of air leads to the formation of a bubbly lubricant. This is a mixture of two distinct fluids, one viscous and quite dense (oil), and the other much less viscous and light (air) [4].

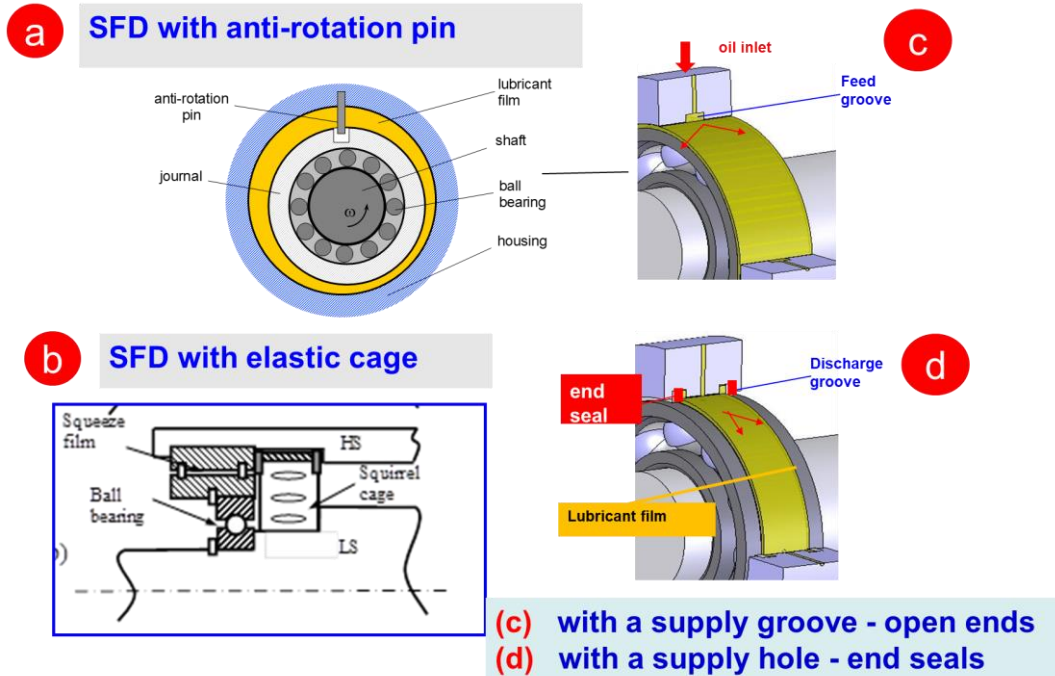


Fig 3. Typical squeeze film damper (SFD) configurations.

Figure 4 shows conceptual views of intershaft dampers for multiple-spool gas turbine engines. These dampers are subject to whirl motions resulting from the combined imbalance response of both low speed (LS) and high speed (HS) rotors. Most SFDs in US aircraft engines incorporate the arrangements in Fig. 4 a & b where the journal (and rolling element bearing) is elastically supported, and the bearing is rigidly attached to the engine frame. The (soft) spring support and SFD *see* the same deflections although the dynamic loads do not divide equally between them.

Dampers in jet engines operate with low magnitudes of external pressurization, max. 3 bar (45 psi) to avoid excessive weight and volume in the lubrication system. Note also that most aircraft engines do not use hydrodynamic journal bearings to avoid the risk of sudden loss of lubrication and to reduce a fluid film bearing induced rotordynamic instability. In some dual shaft jet engines, the inter-spool fluid film bearing, shown in Figure 4a, is known to be a source of such instabilities.

The amount of damping produced is the critical design consideration. If damping is too large, the SFD acts as a rigid constraint to the rotor-bearing system with large forces transmitted to the supporting structure. If damping is too light, the damper is ineffective and likely to permit large amplitudes of vibratory motion with likely subsynchronous motions. Note also that, to be effective, a damping element must be "soft" to allow for rotor motions (or displacements) at the location of the support, in particular while crossing natural frequencies (critical speeds).

The damper geometry (length L , diameter D , and radial clearance c), operating whirl frequency (ω), and fluid physical properties of viscosity (μ) and density (ρ) determine, on first instance, the dynamic forced performance of SFDs. However, there are other important considerations that ultimately determine an appropriate SFD operation. The relevant conditions are:

- kinematics of journal (tied to rotor system and acting forces), in particular the squeeze film velocity $v_s =$ amplitude of motion (r) x whirl frequency (ω).
- magnitude of lubricant supply pressure (P_s) ensuring adequate flow rate and cooling,
- feeding (holes and/or grooves) and end sealing arrangements (O-rings, piston rings, end plates with a gap, etc.)
- fluid inertia effects,
- flow condition: laminar or turbulent.
- type of lubricant dynamic cavitation (vapor or gaseous) and/or air ingestion and entrapment.

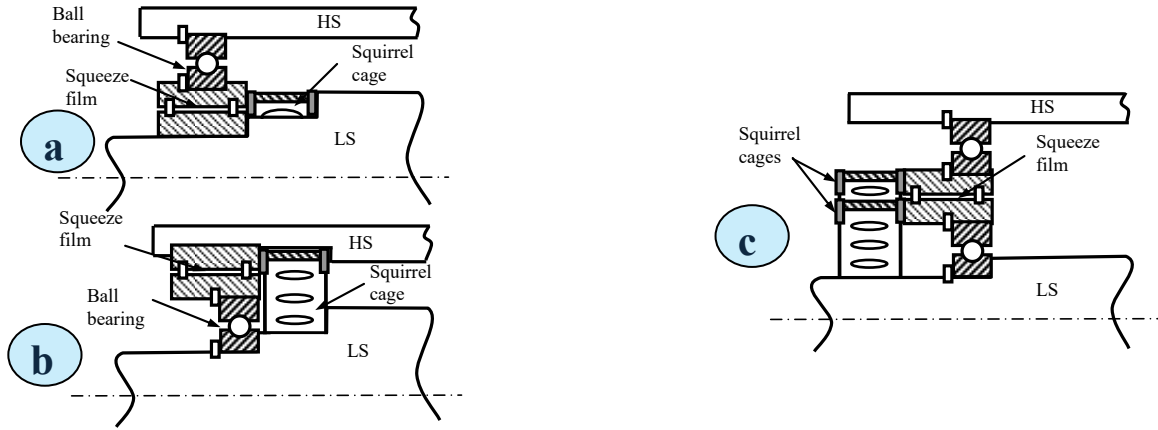


Fig. 4 Schematic views of inter-shaft damper configurations: (a) squeeze film rotates with low speed (LS) rotor, (b) squeeze film rotates with high speed (HS) rotor, and (c) double ball bearing-squirrel cage design.

MODELS FOR PREDICTION OF SFD FORCED PERFORMANCE

In actual practice most dampers are short in axial length, $L/D < 0.50$, and accommodate some type of end seals to increase their damping capability. SFDs include additional features such as high resistance orifices for pressure delivery and discharge and/or deep grooves acting as flow sources or sinks of uniform pressure.

SFD reaction forces and force coefficients are conveniently divided into two major types related to the specific journal center kinematics. For imbalance response analyses, SFD forces are obtained under the assumption of circular centered orbits. The model is applicable when the rotor traverses a critical speed, for example, where the imbalance “force” induces large amplitude orbital motions as the system may have little damping. On the other hand, for rotordynamic critical speed and stability analyses, SFD force coefficients are obtained for small amplitude, journal center motions about a static (equilibrium) position. In the 21st century, computational tools analyze rotor-bearing system transient response events by considering the instantaneous SFD reaction forces, a function of time varying journal kinematics.

Figure 5 depicts a schematic view of a journal whirling within its bearing of diameter $D (=2 R)$. A lubricant of constant density (ρ) and viscosity (μ) fills the radial clearance (c) between the bearing and its journal. The film land length is $L (< D)$. In Fig. 5, Θ and z denote circumferential and axial coordinates attached to the bearing surface; and (X, Y) is a fixed coordinate system for description of the journal kinematics. As the journal whirls, it squeezes the film thickness (h), displaces the fluid, and generates a pressure field (P). The film thickness equals

$$h = c + [e_{Xs} + \Delta e_{X(t)}] \cos\Theta + [e_{Ys} + \Delta e_{Y(t)}] \sin\Theta \quad (1)$$

where (e_{Xs}, e_{Ys}) and $(\Delta e_{X}, \Delta e_{Y}(t))$ are the static and dynamic components of journal motion, respectively. In operation, the journal whirls with a frequency (ω) coinciding with the rotor speed, i.e., synchronous excitation from rotor imbalance, and at other times, with a sub synchronous frequency equaling a system natural frequency, for example.

Unlike in oil lubricated journal bearings, fluid inertia affects the forced performance of a SFD since the SFD clearance (c) is large to allow journal motion and the whirl frequencies are also large [1,2]. The squeeze film Reynolds number $Re_s = [(\rho/\mu) \omega c^2]$ ranges from one to 50 in most practical applications. In general, large clearance SFDs generate significant direct added mass coefficients that may significantly lower the critical speeds of rotating machinery, including aircraft jet engines [1].

Considering temporal fluid inertia¹, the equation governing the generation of dynamic pressure (P) is:

$$\frac{\partial}{R \partial \Theta} \left(h^3 \frac{\partial P}{R \partial \Theta} \right) + \frac{\partial}{\partial z} \left(h^3 \frac{\partial P}{\partial z} \right) = 12 \mu \frac{\partial h}{\partial t} + (\rho h^2) \frac{\partial^2 h}{\partial t^2} \quad (2)$$

¹ Fluid advection, the transport of a flow property by the fluid motion, is also important albeit leading to nonlinear fluid momentum and continuity equations, not a simple Reynolds-like Eq. (2).

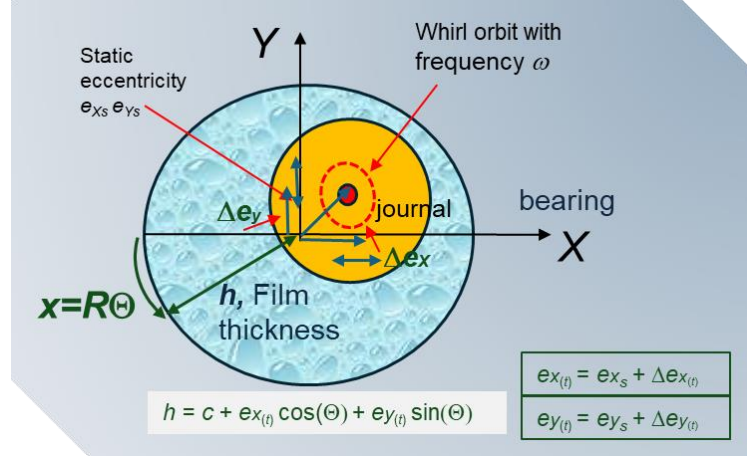


Fig. 5 View of whirling journal and coordinate system for analysis. Exaggerated film thickness.

Eq. (2) applies to an incompressible fluid and is an extended form of the classical Reynolds Eq. [2,3] that includes temporal fluid inertia effects. On the right-hand side of Eq. (2), the first term represents the squeeze film action due to the journal center velocity, and the second term denotes the effects of the journal center acceleration. Above,

$$\frac{\partial h}{\partial t} = [V_X \cos\Theta + V_Y \sin\Theta], \text{ and } \frac{\partial^2 h}{\partial t^2} = [A_X \cos\Theta + A_Y \sin\Theta] \quad (3)$$

where $(V_X, V_Y) = d\Delta e_X/dt, d\Delta e_Y/dt$ and $(A_X, A_Y) = (d^2\Delta e_X/dt^2, d^2\Delta e_Y/dt^2)$ are the components of the journal center velocity and acceleration, respectively.

Numerical solutions to Eqn. (2) with specific boundary conditions and accounting for lubricant cavitation (vapor or gas) are readily available, see for example [7-9]. A later section introduces a detailed physics-based solution model for air ingestion and entrapment. Commercial computational fluid mechanics (CFD) software is also used for prediction of SFD flow and forces, see Ref. [10] (2017). To date, CFD models are off the mark when compared to test data and do not justify the exceptional computing time and engineering effort.

Once found a solution to the elliptical Eq. (2) with appropriate boundary conditions, the integration of the pressure field on the journal surface produces reaction forces,

$$\begin{Bmatrix} F_X \\ F_Y \end{Bmatrix} = - \int_{-L/2}^{L/2} \int_0^{2\pi} P_{(\theta,z,t)} \begin{Bmatrix} \cos\theta \\ \sin\theta \end{Bmatrix} R d\theta dz \quad (4)$$

Open ends SFD dynamic force coefficients for small amplitude motions

SFD reaction forces due to small amplitude journal center motions about a static eccentric or off-centered position, defined as $e_X=e_s$ and $e_Y=0$ as shown in Fig. 6, are of importance in the evaluation of natural frequencies and stability of rotor-bearing systems mounted on dampers with soft or no centering springs. The damper forces are represented in the linearized form,

$$-\mathbf{F} = \mathbf{C}\mathbf{V} + \mathbf{M}\mathbf{A} \rightarrow - \begin{Bmatrix} F_X \\ F_Y \end{Bmatrix} = + \begin{bmatrix} C_{XX} & C_{XY} \\ C_{YX} & C_{YY} \end{bmatrix} \begin{bmatrix} V_X \\ V_Y \end{bmatrix} + \begin{bmatrix} M_{XX} & M_{XY} \\ M_{YX} & M_{YY} \end{bmatrix} \begin{bmatrix} A_X \\ A_Y \end{bmatrix} \quad (5)$$

where (V_X, V_Y) and (A_X, A_Y) are the instantaneous journal center velocities and accelerations along the X and Y directions, respectively. $(C_{\alpha\beta}, M_{\alpha\beta})_{\alpha\beta=X,Y}$ are the damping and inertia (rotordynamic) force coefficients², respectively.

One must emphasize that a SFD does not produce direct stiffnesses (K), i.e., a reaction force opposing a journal center static displacement. That is, given a journal static eccentricity and without rotor spinning, a damper cannot generate a pressure field ($P=0$), hence the static reaction force $\mathbf{F} = \mathbf{0}$. Note that in this case, the right-hand side of Reynolds Eq. (2) is null, hence $P=0$.

² These force coefficients represent changes in forces due to small changes in motion amplitude. This condition usually does not apply to SFDs as they must displace a finite distance to work effectively.

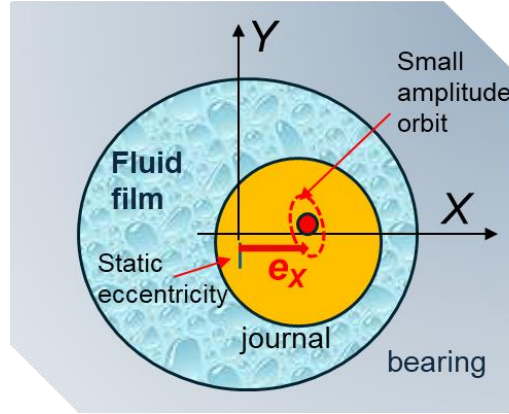


Fig. 6 SFD model: small amplitude journal motions about static off-centered position (e_x). Exaggerated film clearance.

Table 1 lists formulas for the linearized force coefficients for a short length ($L/D < 0.33$), open ends SFD. The coefficients are nonlinear functions of the static³ journal eccentricity ($\varepsilon = e_x/c$). The fluid inertia or added mass coefficients are strictly valid for small to moderate squeeze film Reynolds numbers, $Re_s = (\rho/\mu)\omega c^2 < 10$.

Table 1. Linearized force coefficients for open ends SFD
(STRICTLY VALID) Small amplitude motions about a journal **off-center static** position $\varepsilon=e_x/c$. Source Ref. [1]

Full film model (No oil cavitation)	π -Film Model (Cavitated) (*)
$C_{XX} = \mu D \left(\frac{L}{c}\right)^3 \frac{\pi(1+2\varepsilon^2)}{2(1-\varepsilon^2)^{5/2}}, \quad C_{XY} = 0$	$C_{XX} = \mu D \left(\frac{L}{c}\right)^3 \frac{\pi}{2} \frac{3\varepsilon + i \frac{(1+2\varepsilon^2)}{2}}{2(1-\varepsilon^2)^{5/2}}, \quad C_{XY} = \mu D \left(\frac{L}{c}\right)^3 \frac{\varepsilon}{(1-\varepsilon^2)^2}$
$C_{YY} = \mu D \left(\frac{L}{c}\right)^3 \frac{\pi}{2(1-\varepsilon^2)^{3/2}}, \quad C_{YX} = 0$	$C_{YY} = \mu D \left(\frac{L}{c}\right)^3 \frac{\pi}{4(1-\varepsilon^2)^{3/2}}, \quad C_{YX} = 0$
$M_{XX} = \rho D \left(\frac{L^3}{c}\right) \frac{\alpha \pi [1 - (1-\varepsilon^2)^{1/2}]}{12 \varepsilon^2 (1-\varepsilon^2)^{1/2}}, \quad M_{XY} = 0$	$M_{XX} = \rho D \left(\frac{L^3}{c}\right) \frac{\alpha (i - \pi - 2\varepsilon)}{24 \varepsilon^2}, \quad M_{XY} = \rho D \left(\frac{L^3}{c}\right) \frac{\alpha \left[\ln \left\{ \frac{(1-\varepsilon)}{(1+\varepsilon)} \right\} - 2\varepsilon \right]}{24 \varepsilon^2}$
$M_{YY} = \rho D \left(\frac{L^3}{c}\right) \frac{\alpha \pi [1 - (1-\varepsilon^2)^{1/2}]}{12 \varepsilon^2}, \quad M_{YX} = 0$	$M_{YY} = \rho D \left(\frac{L^3}{c}\right) \frac{\alpha \pi [1 - (1-\varepsilon^2)^{1/2}]}{24 \varepsilon^2}, \quad M_{YX} = 0$

$$i = \frac{2 \cos(-\varepsilon)}{(1-\varepsilon^2)^{1/2}}, \text{ and } \alpha = 1.2-1.0 \text{ for small to moderately large squeeze film Reynolds numbers } (Re_s < 50). \text{ Note } C_{YX} = 0, M_{YX} = 0$$

(*) Take with caution the force coefficients for the π -film damper since oil cavitation (vapor or gas) does not occur for journal motions of (very) small amplitude.

Consider an open ends SFD with length $L=76$ mm (3.0 in), diameter $D=157$ mm (6.18 in), radial clearance $c=0.356$ mm (14 mil), and lubricated with ISO VG 46 oil supplied at 46 °C (115 F). Note $L/D=0.48$ and $D/c=441$. The oil viscosity $\mu=32$ cPoise ($4.64 \cdot 10^{-6}$ psi.s) and density $\rho=860$ kg/m³ (53.7 lbm/ft³). The damper dimensions are adequate for a centrifugal compressor supported on fluid film bearings with a shaft diameter of 100 mm (4 inch). Calculated using the formulas in Table 1, Figure 7 depicts the damping (C) and inertia (M) rotordynamic force coefficients vs. static eccentricity. Recall that these coefficients are derived for small amplitude motions about a static $e_s = e_x$, hence the full film force coefficients are physically sound. Note that $L/D \sim 0.5$, i.e., the geometry is not strictly a short length damper.

Both C and M coefficients are nonlinear, growing rapidly with the (static) eccentricity (e_x/c). $C_{XX} > C_{YY}, M_{XX} > M_{YY}, C_{XY}$

³ Novice practitioners often confuse a static eccentricity (e_s) with the amplitude of whirl motion (r). The latter refers to the amplitude of dynamic motion as the journal describes whirl orbits about a static position. Often $e_s=0$ (centered orbit), whereas r is a non-infinitesimally small amplitude.

$=C_{YX}=0$, and $M_{XY}=M_{YX}=0$. The damping coefficients are large, growing from ~ 80 kNs/m (457 lbf.s/in) to 1 MNs/m (5,710 lbf.s/in) as e_s displaces to 80% of the clearance. The reason for the large growth, 10 times or more the coefficient magnitude at the centered condition $e_x=0$, is the reduction in minimum film thickness, $h_{min} = (c - e_x) = 0.2c = 0.071$ mm (2.8 mil).

Most importantly, the squeeze film added mass coefficients are large in magnitude. At the centered condition ($e_s=0$), M_{XX} and $M_{YY} > \sim 22$ kg (48 lb_m), \sim twice the mass of a solid steel journal, $M_J = \rho_{steel} \pi R^2 L = 11$ kg (24.2 lb_m). The physical mass of fluid in the annular clearance region is just $M_o = (\pi \rho D L c) = 11.5$ gram (0.025 lb_m).

Both SFD practice and the experimental record do not show the large increase predicted by theory. See Ref. [6] for a compendium of experimentally derived force coefficients procured from various SFD configurations. The test data for integral squeeze film dampers (ISFDs) presented later also shows a minor influence of static eccentricity on experimentally obtained damping coefficients.

As stated earlier, the force coefficients in Table 1 are useful to conduct a stability analysis of a rotor-bearing-SFD system. The force coefficients are not intended to model SFDs undergoing large amplitude journal motions, for example whirl orbits with a (finite) sizeable fraction of the damper clearance. That is, the coefficients in Table 1 are not to be used to calculate the synchronous speed rotor response due to mass imbalance.

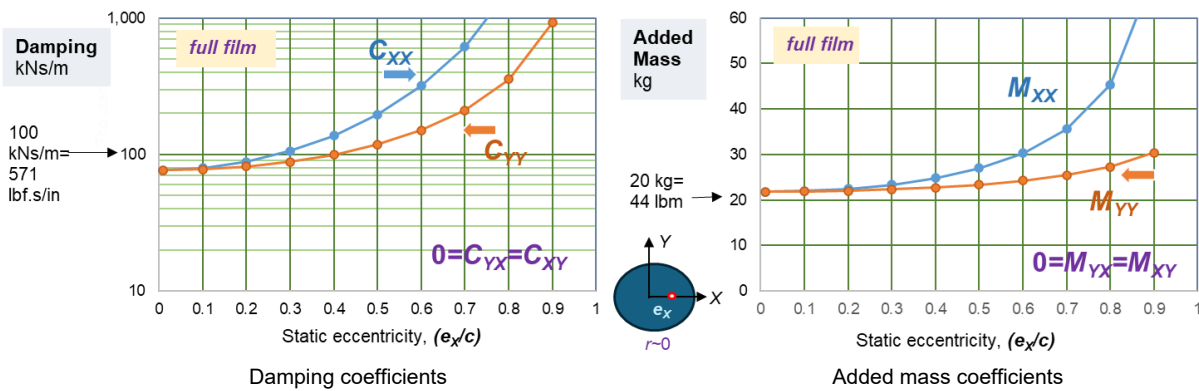


Fig. 7 Open ends SFD: Example of damping and inertia force coefficients vs. static eccentricity (e_x/c). (Very) small amplitude motions about off-centered journal static position. Full film model.

Note 1 MNs/m=5,710 lbf/(in/s) and 60 kg=132 lb_m.

$D=157$ mm (6.18 in), $L=0.48 D$, $c=0.356$ mm (14 mil), $\mu=32$ cPoise ($4.64 \cdot 10^{-6}$ psi.s) and $\rho=860$ kg/m³ (53.7 lb/ft³)

Open Ends SFD dynamic force coefficients for circular orbits

To be effective, SFDs must displace dynamically to generate dissipative (viscous damping) forces. The journal or rotor motions are not typically (infinitesimally) small in amplitude but a sizeable fraction of the film clearance. This condition is particular to operation when a rotor traverses a critical speed, and the excitation source is rotor mass imbalance.

Figure 8 depicts a SFD journal describing circular centered orbits⁴ of amplitude (r) and whirl frequency (ω). The damper generates a constant reaction film force in a reference frame rotating with frequency ω . The radial (F_r) and tangential (F_t) components of the damper reaction force are:

$$F_r = -\{C_{rt} V_t + M_{rr} A_r\}; \quad F_t = -\{C_{tt} V_t + M_{tr} A_r\} \quad (6)$$

where $V_t = (r\omega)$ and $A_r = (-r\omega^2)$ are the journal center tangential speed and radial acceleration, respectively. $V_r = (e\omega)$ is also known as the squeeze film velocity (v_s). (C_{tt} , C_{rt}) are the direct and cross-coupled damping coefficients, and (M_{rr} , M_{tr}) are added mass coefficients, respectively.

Please remember the idealized SFD does not generate a stiffness (K), i.e., a reaction force due to a static journal displacement. The archival literature misleads the practicing engineering when referring to a damper having a radial stiffness, $K_{rr} = (C_{rt} \omega)$. Note K_{rr} is frequency dependent [1,2].

⁴ Circular rotor orbits are typical in rotor-bearing systems with isotropic bearing supports. This is not the case for rotors supported on hydrodynamic journal bearings. However, circular orbits are the easiest to model either analytically or numerically.

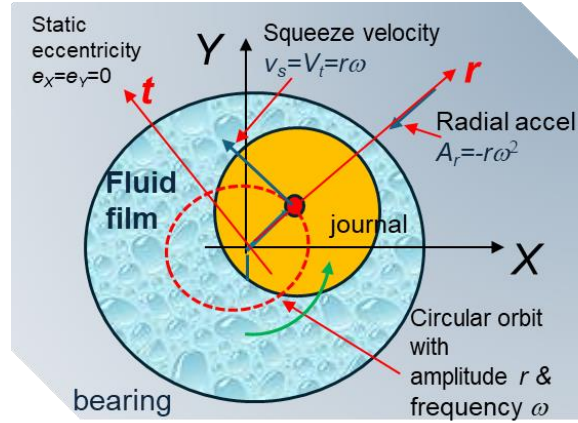


Fig. 8 SFD performing circular centered orbits with frequency ω and amplitude or radius r .

For the short-length, open ends *SFD* model, the force coefficients using the rather simplistic π -film assumption (i.e. half the damper circumference develops liquid cavitation) are [1]:

$$C_{tt} = \frac{\pi \mu D}{4(1-r^2)^{3/2}} \left(\frac{L}{c}\right)^3; \quad C_{rr} = \frac{\mu r D}{(1-r^2)^2} \left(\frac{L}{c}\right)^3 \quad \leftarrow r = r/c \quad (7a)$$

$$M_{rr} = \frac{\pi \rho D}{24} \left(\frac{L^3}{c}\right) \left[1 - 2(1-r^2)^{1/2}\right] \left\{ \frac{(1-r^2)^{1/2} - 1}{r^2 (1-r^2)^{1/2}} \right\}; \quad M_{rr} = -\frac{27}{140 r} \rho D \left(\frac{L^3}{c}\right) \left[2 + \frac{1}{r} \ln\left(\frac{1-r}{1+r}\right)\right] \quad (7b)$$

The orbit amplitude (r) should not be confused with the static journal offset displacement; $e_s=0$, i.e., null in this case. Note that the coefficients in Eq. (7) are not strictly rotordynamic coefficients as their classical definition implies small amplitude motions (infinitesimally small amplitude perturbations) about a journal equilibrium position.

For the full film model (no lubricant cavitation), the direct coefficients (C_{tt} , M_{rr}) equal twice those in Eq. (7), while the cross-coupled coefficients (C_{rt} , M_{rr}) = 0. The added mass coefficients are strictly valid for $Re_s=(\rho/\mu)\omega c^2 < 10$. The full film coefficients are more realistic for circular centered journal motions of small amplitude ($r < 1/4 c$).

Figure 9 depicts the damping and inertia force coefficients for a short length, open ends SFD describing circular centered orbits (CCOs). The damper dimensions and oil properties are identical to those for the results shown in Figure 7. That is, $L=76$ mm (3.0 in), $D=157$ mm (6.18 in), $c=0.356$ mm (14 mil), and $\mu=32$ cPoise ($4.64 \cdot 10^{-6}$ psi.s) and density $\rho=860$ kg/m³ (53.7 lbm/ft³). The figure includes the force coefficients for the full film and the π -film models. Like the linearized force coefficients shown in Figure 7, the coefficients derived for CCOs appear as nonlinear functions of the orbit amplitude (r). Note the large magnitude of direct damping (C_{tt}) even for whirl orbit motions around the centered position ($e=0$).

The rapid growth of the cross-coupled damping coefficient (C_{rt}) is referred as a “stiffness hardening effect,” since some practitioners ascertain $K_{rr}=(C_{rt}\omega)$. K_{rr} is the culprit of severe nonlinear (multiple valued) rotor response accompanied with jump-phenomenon and orbit-instability [1]. However, these effects predicted by overly simple analyses, hardly ever happen in practice.

For a full film condition and $r \rightarrow 0$, the added or virtual mass coefficient $M_{rr} \sim 22$ kg (48 lbm) $> 2 M_J \gg M_o$. The inertia coefficient M_{rr} decreases as the orbit radius increases whereas the direct damping C_{tt} steadily increases. Despite that the fluid mass M_o is just a few grams, M_{rr} can influence the system rotordynamic response as it impacts the location of critical speeds in compact high-speed rotors. The effect is stronger (amplified) for dampers configured with tight end seals.

The open ends SFD physical model dispenses with the means of providing lubricant to the squeeze film land, either via a central feed groove or through orifices. The force coefficients listed in Eqs. (6) and (7) are determined under the assumption of constant viscosity and incompressible lubricant that is supplied with a low (unspecified) supply pressure. The classical model assumes a squeeze film fully submerged in a lubricant bath. That is, a liquid (oil), rather than a gas or ambient air, surrounds the exit sections of the damper. The idealized open ends SFD cannot be implemented in actual practice.

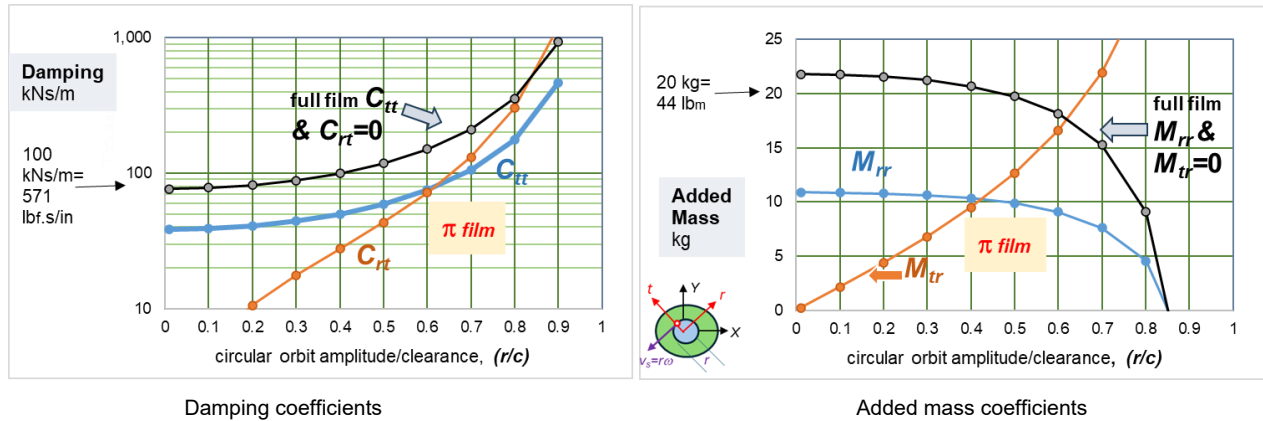


Fig. 9 Open ends SFD: Example of force coefficients vs. amplitude of whirl. Journal describes circular centered orbits. Full film and π film models. Note 1 MNs/m=5,710 lbf/(in/s) and 25 kg=55 lbm.
 $D=157$ mm (6.2 in), $L=0.48 D$, $c=0.356$ mm (14 mil), $\mu=32$ cPoise and $\rho=860$ kg/m³

Figure 10 presents typical experimental damping coefficients obtained for increasing orbit amplitudes and the predictions based on the coefficients listed in Table 1 and Eqs. (7). Reported in Ref. [11] (2010), the experimental C_{tt} , C_{rt} fall in between the π - and full-film predictions. For small whirl frequencies, the oil cavitation zone does not extend over half the damper circumference, and thus the damping coefficients approach the full film prediction. On the other hand, as the whirl frequency increases, the lubricant cavitation zone extends, and the experimental damping coefficients approach those derived for the π -film model. It is most important to note that the experiments in [11] were conducted with a damper fully submerged in a lubricant bath. The test rig closed any paths that would permit the ingestion and entrapment of air. This condition is most difficult to achieve in practice.

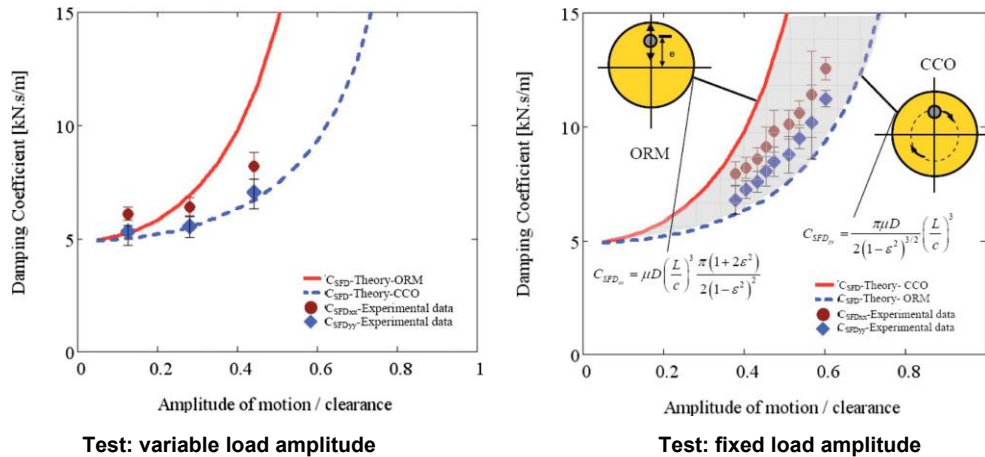


Fig. 10 Open ends SFD: experimental damping coefficients vs. journal motion amplitude. Data from [11] (2010) for multiple frequency sweep loads (30-120 Hz) with fixed or variable load amplitude. Compare with predictions from full film model: circular centered orbit (CCO) and motions about off-centered static position (ORM).
 $D=127$ mm (5.0 in), $L=1/5 D$, $c=0.125$ mm (5 mil), $\mu=3$ cPoise ($0.43 \cdot 10^{-6}$ psi.s) and density $\rho=860$ kg/m³ (53.7 lbm/ft³)

A brief discussion follows on finite length SFD configurations, some with central feed grooves, and operating conditions that affect the forced performance of the mechanical element.

Force coefficients for finite length SFDs

There are also equations applicable to finite length SFDs, i.e., (L/D) not small. For a full film, open ends SFD and small amplitude whirl motions ($r/c < 0.25$), Reinhart and Lund [12] (1975) derive:

$$C_{xx} = C_{yy} = C_{ii} = 12\pi \frac{\mu R^3 L}{c^3} \left[1 - \frac{\tanh(L/D)}{(L/D)} \right] \quad M_{xx} = M_{yy} = M_{rr} = \pi \frac{\rho R^3 L}{c} \left[1 - \frac{\tanh(L/D)}{(L/D)} \right] \quad (8)$$

Note that the damping coefficient is proportional to (μ/c^3) whereas the inertia coefficient varies with (ρ/c) . The added mass coefficient is always present; that is, it is a physical property of the squeeze film. Its influence on the dynamics of a rotor-bearing system, however, becomes dominant at high whirl frequencies, i.e., when the rotor acceleration $A_r = |-r\omega^2|$ is large. At these operating conditions, the inertia force $|M_{rr}A_r|$ is of the same order or even larger than the viscous (damping) force $|C_{ii}V_i|$, where $V_i = v_s = (r\omega)$ is the squeeze velocity.

Fully sealed vs. open ends SFDs: comparison of their damping performance

Formulas for the prediction of SFD force coefficients with tight end seals can be easily derived from Eq. (8) by assuming an infinitely long bearing ($L/D \gg 0$). $\left[1 - \frac{\tanh(L/D)}{(L/D)} \right]_{L/D \rightarrow \infty} = 1$ emulates a damper with no lubricant leakage through its ends. In this case, the squeeze film pressure field does not vary axially, and the damper produces a large reaction force despite its finite physical length. The damping and virtual mass coefficients for a fully sealed SFD are:

$$(C_{xx} = C_{yy} = C_{ii})_{sealed} = \frac{12}{8} \pi \frac{\mu D^3 L}{c^3} \quad (M_{xx} = M_{yy} = M_{rr})_{sealed} = \pi \frac{\rho D^3 L}{8c} \quad (9)$$

The coefficients above are valid for $r \rightarrow 0$ and a full film condition. Eq. (9) ignores the effect of either feed and/or discharge holes, i.e., any means to supply and drain the lubricant into/from the squeeze film land. From Eq. (8), as $L/D \rightarrow 0$, the force coefficients for the open ends (short length) SFD are:

$$(C_{xx} = C_{yy} = C_{ii})_{open} = \frac{1}{2} \pi \frac{\mu D L^3}{c^3}; \quad (M_{xx} = M_{yy} = M_{rr})_{open} = \frac{1}{24} \pi \frac{\rho D L^3}{c} \quad (10)$$

Hence, the ratio of force coefficients (sealed ends/open ends) equals

$$\left. \frac{C_{sealed}}{C_{open}} \right]_{xx,yy} = \left. \frac{M_{sealed}}{M_{open}} \right]_{xx,yy} = \frac{3}{(L/D)^2} \quad (11)$$

That is, for a damper with $L/D=1/5$, a fully sealed damper construction amplifies the damping coefficient by $(3 \times 5^2) = 75$ times when compared to the open ends configuration! Note the added mass coefficient also increases in an identical proportion.

Effect of feed grooves on SFD force performance

Some dampers are designed with feed and/or discharge grooves to ensure a continuous flow of lubricant through the squeeze film lands. Figure 11 shows schematic views for two typical configurations. A groove is thought to provide a uniform flow source with constant pressure around the bearing circumference. A central feed groove also divides the flow region into two separate squeeze film dampers working in parallel, i.e., the reaction forces from each film land add.

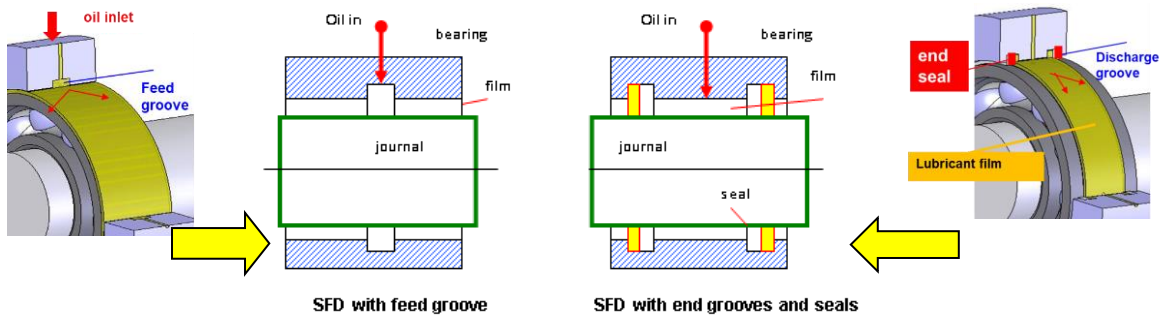


Fig. 11 Schematic views of typical grooved SFD configurations: with central feed groove and with end grooves for seals installation.

For the open ends SFD with a central groove SFD and having two adjacent film lands of length L , theory predicts force coefficients about one-fourth those for a SFD with twice the land length ($=2L$) and no central groove. This is so since the damper reaction force for the no groove configuration $\sim (2 \times L)^3 = 8L^3$, and the force for the grooved damper $\sim (2 \times L^3)$.

Experiments and field performance, however, demonstrate that grooved dampers generate much larger forces than those derived from simple open ends SFD theory. Ramli et al. [13] (1987) first reported that experimentally obtained force coefficients are significantly higher in magnitude, in some cases by a factor of 10, than predictions based on short length bearing theory. Later, Zeidan et al. [4] (1996) and San Andrés et al. [6] (2016) also measured sizeable amplitude dynamic pressures in a deep groove connecting two adjacent squeeze film lands and found damping and added mass coefficients larger than a simple theory predicts.

Figure 12 shows a schematic view of the flow region that includes a deep feed groove and adjacent film lands. Taken from Ref. [6] (2016), the figure includes measured dynamic pressures in the groove that are as large as those in the thin film section. Note that in the test SFD, the depth of the groove is 9.5 mm (3/8 inch) $\sim 70 \times c = 0.135$ mm (5.3 mil). The test section has two film lands, each with $L = 25.4$ mm (1 inch), located on the sides of the feed groove whose axial extent $= \frac{1}{2} L$ (0.5 inch).

Ref. [14] (2010) presents an original fluid inertia model for prediction of the forced response of grooved SFDs and oil seal rings with internal (feed) grooves. Predictions based on an effective groove depth are in good agreement with experimental oil seal rings' force coefficients reported by Childs et al. (15) [1997]. The effective groove depth ranges from 5 to 20 times the film radial clearance (c), irrespective of the groove physical depth, one order of magnitude larger or more than the film clearance.

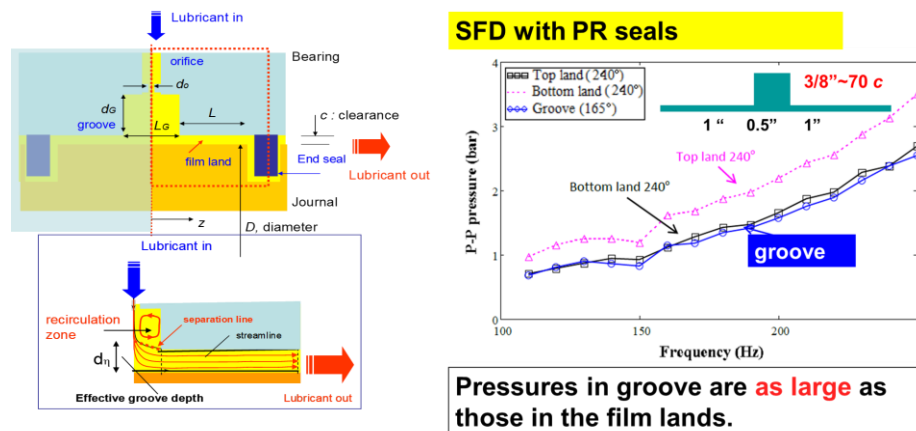


Fig. 12 SFD with central feed groove and sealed with piston rings (PR). Measured peak-peak pressures in film and groove. Data reproduced from Ref. [6] (2016).

$D=127$ mm (5.0 in), $L=1/5 D$, $c=0.135$ mm (5 mil), $\mu=3$ cPoise and density $\rho=800$ kg/m³.
Groove depth = 9.5 mm (3/8 inch) $\sim 70c$, width = 12.7 mm (1/2 inch) $= \frac{1}{2} L$.

Effect of end seals on SFD forced performance

SFDs usually include some type of end seals to reduce the through flow and to amplify the available viscous damping coefficient for energy dissipation. Figure 13 depicts schematic views of the most common end seal configurations: O-rings (OR), piston rings (PR), and end plate (gap) seals. SFDs in commercial jet engine rotors incorporate PR as end seals; and OR in military aircraft gas turbine engines [6]. However, O-ring cocking and locking with a resulting excessive oil leakage is a pervasive problem. Implementing patented (proprietary) designs seems to resolve the reliability issue, see Ref. [6] (2016).

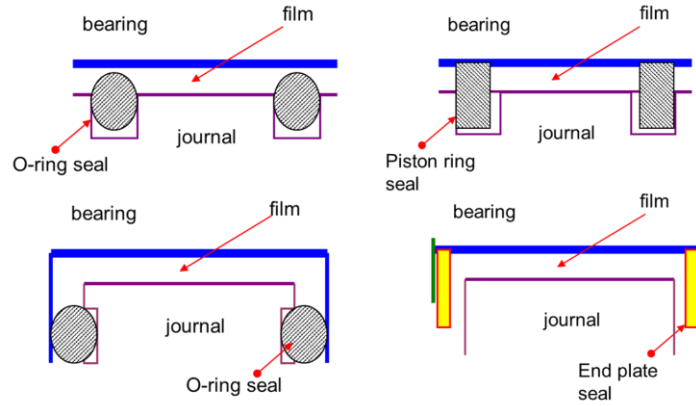


Fig. 13 Schematic views of end seals for SFDs: O-rings, piston rings, and end plate seals.

Many industrial compressor applications implement OR as end seals due to their ready availability and tight sealing. However, these applications are restricted to low static loads and room temperature conditions. OR do add viscous damping, albeit with a magnitude lower than the damping coefficient from the squeeze film. Material compatibility of the O-rings with the lubricant and gas external medium is a design consideration. Material aging, temperature degradation, long-term relaxation, and creep of elastomeric OR when supporting large static loads are issues easily overlooked. The oversight could prove consequential in a high-pressure barrel compressor, for example. In addition, the assembly compression of the O-rings in their sitting grooves is important. If a ring fits loosely in its groove, the lubricant easily leaks and draws in air (gas) from the environment. If the ring is too tight, on the other hand, then large (sliding) friction forces quickly wear out the elastomeric element. Incidentally, too large amplitude of whirl motions can also produce a transient decompression of the O-ring which permits intermittent ingestion of air into the squeeze film. Under large whirl amplitudes induced by high loads, the OR polymeric inner structure bonds break down so extensively that the reformation is much slower than the strain cycle time, thus leading to a reduction in O-ring stiffness and small damping. That is, the decrease of an O-ring stiffness and damping obeys to the elastomer material relaxation and recovery times being longer than the period of whirl motion.

The design of an end seal demands of an empirical flow coefficient extracted from exhaustive experimentation. Figure 14 depicts two idealized end flow restrictions, one could be construed as a piston ring, and the other as an end plate seal. The gap (b) and length (l) of the restrictor control the lubricant exit flow to an ambient condition. The restriction is modeled as a resistance (R_{seal}) to the local exit flow $q_{end} \sim \frac{1}{2} Q_{oil}/(\pi D)$ and due to the pressure drop (ΔP_{end}). That is,

$$q_{end} = \frac{\Delta P_{end}}{R_{seal}} = C_{seal} \Delta P_{end} \leftarrow C_{seal} \sim \frac{1}{12 \mu} \left(\frac{b^3}{l} \right) \quad (12)$$

C_{seal} is construed as a local flow conductance with units of $[(m^2/s)/Pa]$. Note that $C_{seal}=0$ ($R_{seal} \gg 0$) makes a very tight end seal, one without side flow. On the other hand, $1/C_{seal} = R_{seal} \rightarrow 0$ represents an open ends condition. Eq. (9) rarely delivers accurate results, hence the need for measurement of the flow and pressure drop across the end seal [6]. Incidentally, note that Eq. (9) assumes $\Delta P_{end} > 0$, and avoids the definition of air ingestion for the case of subambient pressures, i.e., when $\Delta P_{end} < 0$.

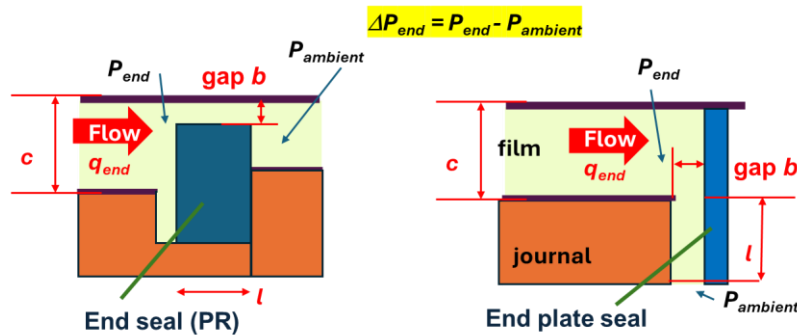


Fig. 14 Schematic idealized views of the exit flow through an end seal (restriction): piston ring (left graph) and end plate seal (right graph).

End plate seals are commonly used in integral squeeze film dampers (ISFDs). The axial gap (b) between the journal and the side plate is a crucial design consideration, see the right-side graph in Figure 14. If $b \gg c$, the lubricant leaks easily and the damping coefficient decreases. On the other hand, if $b < c$, a tight seal, the damping coefficient quickly grows; albeit as the leakage reduces, thermal and elastic effects may affect the performance of the mechanical element. One should also expect a significant growth in the inertia force coefficients as the end gap reduces.

In an actual SFD, the supplied lubricant (Q_{oil}) flows through one or more feed holes or ports, fills in a central groove, displaces throughout the film lands, and then leaves the damper through the end seals, if applicable, or through exit holes. Figure 15 shows a descriptive view of the hydraulic network of the fluid flow across a SFD. The static pressure drop, supply minus discharge, pushes the flow (Q_{oil}) to overcome the various flow resistances. The overall resistance (R_{flow}) adds the individual resistances from the holes (R_{holes}), lands with small film clearance ($R_{land} \sim (\mu/c^3) L/(\pi D)$), and the end seals (R_{seals}). The resistance of the end seals is typically extracted from the supplied flow vs. static pressure measurements.

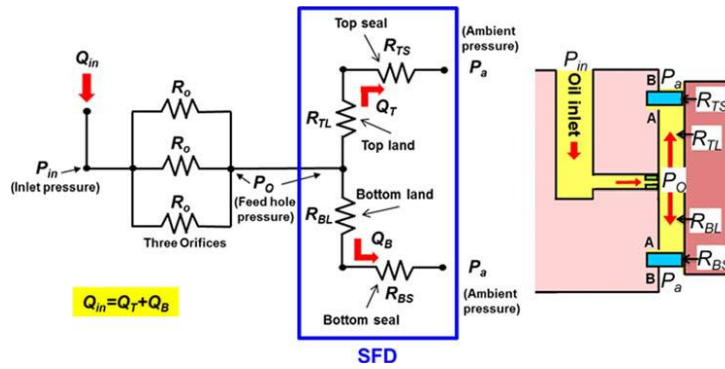


Fig. 15 Typical flow diagram with hydraulic resistances representing a sealed ends SFD.

Later this tutorial shows a comparison of experimental force coefficients obtained for two sealed ends SFDs having the same physical dimensions, oil properties, and operating conditions in whirl frequency and orbit radius. One damper is sealed with piston rings (PR) whereas the other damper hosts O-rings (OR). The tutorial closes with experimental force coefficients for an ISFD applicable to a hydrocarbon gas compressor.

Power dissipation in an SFD

A SFD dissipates power (ϕ) due to the action of its viscous (damping) forces. The viscous power equals

$$\phi = \mathbf{V}^T \mathbf{C} \mathbf{V} = [V_X \quad V_Y] \begin{bmatrix} F_X \\ F_Y \end{bmatrix} = -[V_X \quad V_Y] \begin{bmatrix} C_{XX} & C_{XY} \\ C_{YX} & C_{YY} \end{bmatrix} \begin{bmatrix} V_X \\ V_Y \end{bmatrix} = -(C_{XX}V_X^2 + C_{YY}V_Y^2 + [C_{XY} + C_{YX}]V_YV_X) \quad (13)$$

and for a circular centered orbit with amplitude r and frequency ω , $\phi = -(C_u v_s^2) = -C_u r^2 \omega^2$.

For the example open ends SFD presented in Fig. 7, take an amplitude of whirl $r=0.2 c=0.71$ mm (3 mil) and $C_{it}=100$ kNs/m (571 lb_f.s/in), then at a frequency of $\omega=150$ Hz (9 krpm), the squeeze velocity $v_s=67$ mm/s (2.6 in/s), and the dissipated power $\phi=0.45$ kW = 0.6 HP. The small magnitude of ϕ will likely not affect the performance of the rotating system. However, if the damper should be tightly sealed, as the damping coefficient (C_{it}) grows with the ratio $3(D/L)^2$, then ϕ would increase by 75 times. Such a damper configuration would be a poor choice, and not even accounting for the severe thermos-elastic effects induced by such an excessively large magnitude damping, $C_{it}=7,500$ kNs/m (42,825 lb_f.s/in)!

In the author's experience at the laboratory, supplied with enough flow, SFDs do not overheat, and the oil viscosity remains nearly constant. In other words, the viscous power penalty is rather a secondary consideration when designing the damper with adequate means to feed, circulate and remove the lubricant.

Lubricant cavitation vs. air ingestion and entrapment in SFDS

Zeidan et al. [4] (1996) identify SFD operation with distinct types of fluid cavitation (vapor or gas), and a regime due to air ingestion and entrapment. The appearance of a particular condition depends on the damper type (sealed ends or open to ambient),

the magnitude of supply pressure (P_s) and flow rate (Q_{oil}), whirl frequency (ω), and the magnitude of dynamic load producing (small or large) journal displacements ($e_{(t)}$) within the film clearance. The squeeze film velocity $v_s = (r\omega)$ is the most important journal kinematics parameter.

Gas cavitation following the journal motion appears in ventilated (open ends) SFDs operating at low frequencies and with small to moderate journal amplitude motions, i.e., small v_s . A well-defined cavitation *bubble* containing the release of dissolved gas in the lubricant or air entrained from the vented sides follows the whirling motion of the journal. In other words, the cavitation zone appears steady in a rotating frame. The traveling gas bubble appears not to affect the generation of the squeeze film pressure in the full film zone. The persistence of this cavitation regime upon reaching steady operating conditions (high frequencies) in an aircraft application is remote.

Lubricant vapor cavitation appears in dampers with tight end seals that prevent entrainment of the external gas media and for operation with a sufficiently large supply pressure. In this last case, the through oil flow also prevents the ingestion of air. Furthermore, the lubricant must be relatively free of dissolved gases such as air, a condition not readily found in practice⁵.

Figure 16(a) depicts the measured dynamic film pressure waves vs. time in a damper that developed lubricant vapor cavitation. Taken from Ref. [16] (2001), the graphs illustrate the variation of dynamic squeeze film pressure and gap (film thickness) for five periods of journal orbital motion. The radial clearance is $c=0.343$ mm (13.5 mil). The whirl frequency $\omega=75$ Hz, and the centered journal orbit amplitude $r=0.180$ mm (7 mil) $=0.52c$. The squeeze film velocity is $v_s=(r\omega)=84$ mm/s (3.3 in/s). The oil supply pressure $P_s=1.45$ bar (21.3 psig), and the discharge is ambient to a pool of liquid. That is, the damper is fully submerged in a lubricant bath. Note that the pressure profile is smooth and shows nearly identical shapes for each consecutive period of motion. A (flat) constant pressure zone develops at nearly zero absolute pressure, and it corresponds to the rupture of the film and formation of a vapor filled cavity. The cavity appears only during that portion of the journal motion cycle where the film gap increases. The vapor bubble collapses immediately as the local pressure rises above the lubricant vapor pressure. In general, correlation of measured pressures and vapor cavitation extent against predictions based on film rupture models are satisfactory.

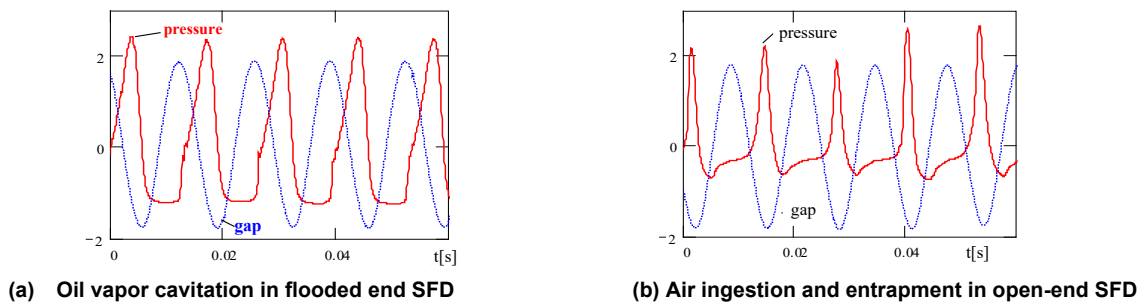


Fig. 16 Dynamic film pressure (bar) and local film gap (mm x 10). (a) flooded SFD with vapor cavitation, (b) SFD venting to air and pressure profile showing air ingestion. Taken from Ref. [16] (2001).

Air ingestion and entrapment persists in vented (or open ends) dampers operating at high squeeze velocities. A low magnitude supply (feed) pressure pushes a small throughout flow rate that cannot overcome the fast changes in film land volume. Figure 16(b) depicts the measured film dynamic pressure versus time in a SFD showing pervasive air entrainment. The operating conditions are identical to those for the measurements depicted in Figure 16(a), except that the damper end opens to atmospheric conditions, i.e., not submerged in an oil bath. A suction pressure draws air into the thin film at the locations where the local film gap is increasing. The cyclic fluid motion leads to air entrapment, with *bubbles* remaining in the zones of dynamic pressure generation above ambient. Air ingestion forms intermittent air fingering surrounded by liquid striations, see the photographs in Fig. 17 for vivid details. These islands of air may shrink, break up into smaller zones, or diffuse within the lubricant. The size and concentration of the ingested air fingers depend on the journal squeeze velocity and the supplied flow rate. The fluid at the damper discharge is cloudy and foamy.

The film dynamic pressures with air entrainment, Figure 16(b), show important distinctions when compared to those pressures induced by lubricant vapor cavitation, Figure 16(a). With air ingestion, the film pressures differ markedly from one period to the next, the peak pressures show large variations and evidence pressure spikes as gas bubbles collapse. Furthermore, the pressure flat zone is nearly at ambient pressure. Note that occasionally subambient film pressures appear.

⁵ All oils as manufactured have a sizable percent of dissolved gases, typically 4% to 6% in volume.

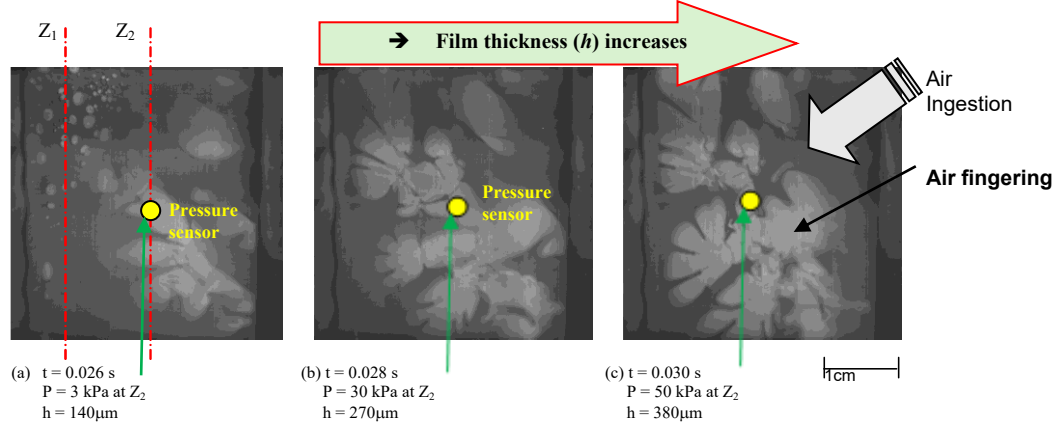


Fig. 17 Photographs of SFD flow field with air ingestion and entrapment. Tests with whirl frequency at 25 Hz and feed pressure 1.93 bar. Elapsed time for photographs is 2 ms (whirl period = 40 ms). Taken from Ref. [16] (2001).

Inevitably, the vast majority of SFDs operate with foam-like fluids (bubbly mixtures) considering the low magnitude of pressure supply (small through flow rate), large damper clearances, and high operating whirl frequencies, i.e. typically large squeeze velocities. Of course, mixed operation regimes can also occur in practice. For instance, tightly sealed dampers may show both air entrainment and oil vapor type cavitation where gas fingers may coexist around a large bubble containing vapor lubricant. Note that the entrapment of air delays the increase of squeeze film pressures since there is less liquid filling the damper film clearance.

Ultimately, air entrainment into the squeeze film lands is device dependent, and its severity increases with the amplitude and frequency of journal motion. That is, v_s is the fundamental variable. Air ingestion can be prevented by increasing the lubricant supply pressure to ensure a sufficiently large throughout lubricant flow. The recommendation is impractical for aircraft engines where weight and oil storage volume are at a premium.

A 21ST CENTURY PREDICTIVE MODEL FOR SFD FORCED PERFORMANCE

San Andrés and Koo [8] (2020) advance a sound model for SFDs dampers sealed with piston rings (PR) and operating with a homogenous bubbly mixture of air in oil, i.e., a compressible fluid. Air is drawn into the film through regions of low pressure, either the ends open to ambient air or through the slits of PR, for example. The governing equation for the generation of squeeze film pressure (P) is:

$$\frac{\partial}{R \partial \Theta} \left(\frac{\rho_m}{12 \mu_m} h^3 \frac{\partial P}{R \partial \Theta} \right) + \frac{\partial}{\partial z} \left(\frac{\rho_m}{12 \mu_m} h^3 \frac{\partial P}{\partial z} \right) = \frac{\partial (\rho_m h)}{\partial t} + \left(\frac{\rho_m h^2}{12 \mu_m} \right) \frac{\partial^2 (\rho_m h)}{\partial t^2} \quad (14)$$

The mixture density ρ_m and viscosity μ_m , depend on the local gas (air) volume fraction (GVF) β ,

$$\rho_m = \rho_g + (1 - \beta) \rho_{oil} \sim \alpha \rho_{oil}; \quad \mu_m = \mu_g + (1 - \beta) \mu_{oil} \sim \alpha \mu_{oil} \quad (15)$$

with $\alpha = (1 - \beta)$ as the liquid volume fraction (LVF). The approximate expressions on the right side of Eq. (15) follow since $\mu_{oil} > \mu_g$ and $\rho_{oil} \gg \rho_g$. The GVF (β) depends on the pressure (P) as,

$$\beta_{(P)} = 1 - \alpha_{(P)} = \frac{1}{1 + \frac{P_{(\Theta, z, t)} - P_v}{P_s - P_v} \left(\frac{1 - \beta_s}{\beta_s} \right)} \quad (16)$$

where β_s is known at the supply pressure P_s , and $P_v \sim 1$ kPa (0.145 psi) is the lubricant vapor pressure. Note the model relies on a known state (β_s, P_s), difficult to quantify until recently.

Through a feedhole with diameter ϕ_m and located at $\{\Theta_{in}, z=z^*\}$ the delivered mass flow of lubricant is

$$\dot{M}_{in} = (\rho Q)_{in} = C_d \left(\frac{1}{4} \pi \phi_m^2 \right) \sqrt{2 \rho_m (P_s - P_{(\Theta_m, z^*, t)})} \quad (17)$$

where C_d is an empirical orifice loss coefficient. The equation above applies only when $P_s > P_{film}$; otherwise $\dot{M}_{in} = 0$; hence

emulating the operation of a mechanical check-valve.

Conventional analyses typically model the outflow through end seals as proportional to a local pressure drop ($P_{end}-P_a$) and an (empirical) end seal coefficient, i.e., $q_{end} = C_{seal} \Delta P_{end}$, Eq. (12). The overly simplistic model does not apply to a piston ring (PR) as the experimental record shows a jet-like outflow through the PR slits. As shown schematically in Figure 18, the mass flow through a PR slit with area A_{slit} equals

$$M_{exit} = C_{slit} A_{slit} \sqrt{2\rho \left| P_{(\theta_{slit}, \frac{1}{2}t)} - P_a \right|} \quad (18)$$

that allows for the outlet and inlet flows of a mixture through the PR slit opening.

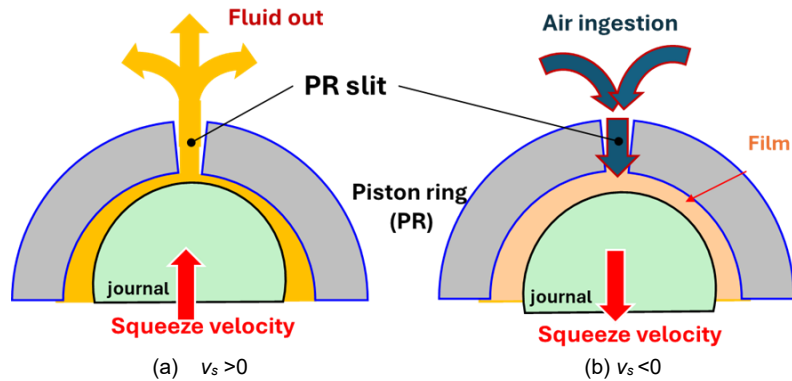


Fig. 18 Depiction of flow through a piston ring (PR) slit. (a) Fluid leaves as journal approaches PR slit ($v_s > 0$), and (b) air is drawn as journal reverses motion ($v_s < 0$).

There are more advanced models that include a transport equation for the GVF; see Gehannin et al. [17] (2016) in France, and Ref. [9] (2023). In Italy, Geller et al. [18] (2022) reproduce the model developed in this section.

Appendix A displays video recording evidence of air ingestion and entrapment along with recorded dynamic pressures in the squeeze film land of a test SFD. In the model, the greatest unknown relates to the quantification of the gas volume fraction (β), an outcome of the squeeze film kinematics and end seal conditions. Rodriguez and San Andrés [19] (2024) resolved the hurdle in a surprisingly simple way. A procedure draws a sample of the bubbly fluid into a balloon; and by measuring the volume and weight of the inflated balloon produces an accurate estimation of the ingested GVF.

Figure 19 shows the measured GVF (β) vs. squeeze film velocity ($v_s = r\omega$) obtained in a tight O-rings sealed SFD lubricated supplied with a low pressure, $P_s = 0.69$ bar(g). The SFD clearance $c = 0.279$ mm (11 mil), $L = 25.4$ mm (1 inch), and $D = 5L$. During the measurements, the circular centered orbits had amplitudes ranging from $r = 0.20c$ to $0.45c$, and the whirl frequency reached 70 Hz. Note the GVF, i.e., the amount of air ingested, increases as v_s grows above a threshold magnitude ~ 25 mm/s (1 inch/s). At the largest $v_s = 55$ mm/s ($r = 0.45c$ and $\omega = 70$ Hz), the amount of air ingested is $\sim 58\%$. At this operating condition, the lubricant leaving the damper through a discharge hole is just a foamy mixture. While undergoing large orbital motions and frequencies, the OR lose their assembly compression pressure and allow for air ingestion; lots of it!

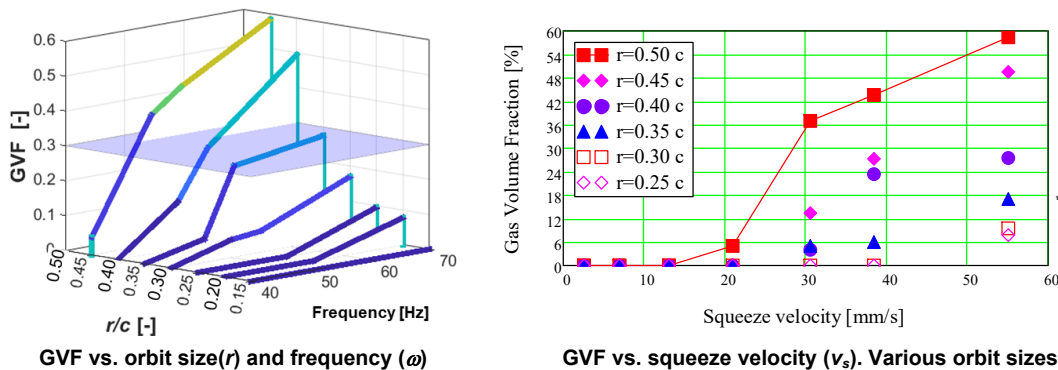


Fig. 19 O-ring sealed-SFD supplied at 0.69 bar(g): Quantified gas volume fraction (GVF) vs. squeeze velocity ($v_s = r\omega$) and orbit amplitude (r/c). Whirl frequency 70 Hz max. Data from Ref. [19] (2024).

THE EXPERIMENTAL RECORD FOR SEALED SFDS: PISTON RINGS VS O-RINGS

Appendix B presents the SFD test rig at Texas A&M University and details the procedure for the experimental identification of force coefficients from journal orbital motions of sizeable amplitude, centered or off-centered, rather than (infinitesimally) small amplitude journal motions, as classical theory requires.

Throughout a decade long research effort sponsored by a major aircraft engine manufacturer, the test rig hosted several damper configurations featuring short and long film land lengths, with and without feed and/or discharge grooves, with one, two or three feed holes, with open ends, and end sealed with either piston rings (PR) or O-rings (OR). Distinct journals also enabled the assembly of dampers with various clearances (c), some tight (5 mil) and others large (15 mil). Ref. [6] (TPS 2016) details the experimental identification of force coefficients for centrally grooved SFDs with open ends and sealed with PR.

Figure 20 shows a cross-section of the test rig housing OR, and Table 2 lists the geometry, lubricant type and operating conditions. During controlled single-frequency dynamic load tests, shakers drive the test rig into motion, typically circular orbits, centered and off-centered. Measured applied forces and ensuing bearing displacements leads to the estimation of SFD force coefficients over a frequency range.

Table 2. SFD test rig dimensions and operating conditions. Taken from Refs. [19,20]

Geometry	SI unit	US unit	ISO VG 2 oil	SI unit	US unit
Land length, L	25.4 mm	1 inch	Viscosity, μ	2.7 cPoise	$3.91 \cdot 10^{-7}$ psi.s
Diameter, D	127 mm	5 inch	Density, ρ	800 kg/m^3	40.9 lb/ft^3
Radial clearance, c	0.373 mm	14.7 mil	$\nu = \mu/\rho$	$3.51 \cdot 10^{-6} \text{ m}^2/\text{s}$	$5.44 \cdot 10^{-3} \text{ in}^2/\text{s}$
Whirl frequency, ω	10-100 Hz		Supply pressure, P_s	0.69 – 6.9 bar	10-100 psig
Orbit amplitude, r	0.05 c -0.45 c				
Max. squeeze velocity, v_s	70 mm/s	2.5 in/s	Reynolds number, Re_s	$(\rho/\mu) \omega c^2$	Max. 26

For reference, using Eq. (9), the theoretical damping and inertia force coefficients for a fully sealed SFD are $C^* = 12.76 \text{ kNs/m}$ ($72.8 \text{ lb}_f\text{s/in}$) and $M^* = 44 \text{ kg}$ (97 lb_m). Remember, formulas in Eq. (9) ignore the effect of feed holes and do not allow for lubricant through flow.

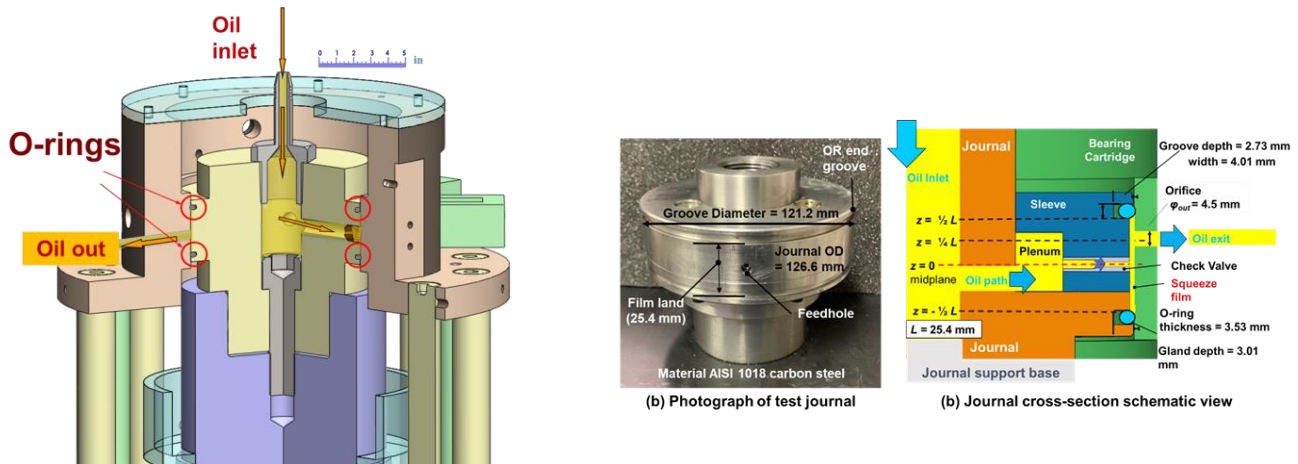


Fig. 20. Test OR-SFD: 3D cross section with lubricant flow path and views of journal and O-rings installed.

Effect of supply pressure on the force coefficients of two sealed ends SFDs

For centered whirl orbits with amplitude $r/c = 0.3$, Figure 21 presents the experimental⁶ SFD direct damping $C = \frac{1}{2} (C_{XX} + C_{YY})$ and added mass $M = \frac{1}{2} (M_{XX} + M_{YY})$ coefficients for the two test dampers as the oil supply pressure (P_s) increases. During the tests reported in Ref. [20] (2019), the maximum squeeze film speed = 70 mm/s (2.75 in/s) and the largest squeeze Reynolds #, $Re_s \sim 26$.

⁶ Vertical bars denote the uncertainty in the estimation of the force coefficients.

For the PR-SFD, direct damping (C) increases 30% as P_s grows from 2.1 bar (31 psig) to 6.2 bar (91 psig), whereas the virtual mass (M) stays nearly constant at ~ 30 kg (66.1 lbm). For the OR-SFD, C increases $\sim 11\%$ as P_s increases and M decreases $\sim 13\%$. The added mass (M) for the OR-SFD is 16% larger than that of the PR-SFD. In short, for $P_s > 2$ bar (28.8 psig) the OR-SFD produces slightly $\sim 11\%$ more damping than the PR-SFD does since the O-rings provide a perfect seal (no leakage).

As per comparison with the fully sealed force coefficients calculated from Eq. (9), the experimental C approaches the theoretical magnitude (C^*) as the oil supply pressure increases. The added mass coefficient is $\sim 60\%$ of the prediction (M^*) but still having a large magnitude, nearly twice the mass of the bearing cartridge ($M_{BC}=15.6$ kg). The PR allow leakage through the slits made by their abutted ends. Note that the damping discussed above is only the viscous portion. The OR-SFD produces $\sim 10\%$ more damping after adding the damping from the viscoelasticity of the OR; see Refs. [24] (2019), [25] (2019), [26] (2021), and (27) ([2024) for more details on the identified force coefficients for a SFD sealed with PR and with OR.

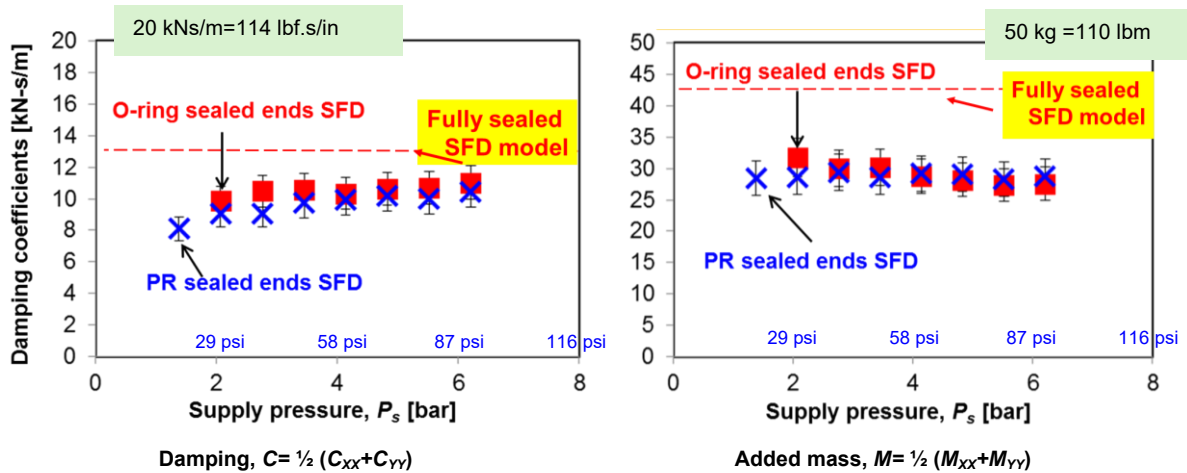


Fig. 21 OR-SFD vs. PR-SFD: direct damping (C) and added mass (M) coefficients vs. lubricant supply pressure (gauge). Circular centered orbits with amplitude $r = 0.3c$ and whirl frequencies 10 - 100 Hz. (Three feedholes). Fully-sealed SFD: $C^*=12.76$ kNs/m (72.8 lbf.s/in) and $M^*=44$ kg (97 lb_m). Taken from Ref. [20].

Note the experimental force coefficients are different from the ideal predictions $C^*=12.76$ kNs/m (72.8 lbf.s/in) and $M^*=44$ kg (97 lb_m) because the test dampers have feed holes acting as sources of constant pressure whereas the PR-slits and exit hole in the OR-SFD act as (local) sinks of flow. Both inlet and exit conditions contribute to distort the squeeze film pressure field making it markedly different from the idealized SFD.

Effect of static eccentricity and orbit amplitude on the force coefficients of two sealed ends SFDs

Figure 22 shows the experimental damping (C_{xx} , C_{yy}) and added mass (M_{xx} , M_{yy}) coefficients for both dampers supplied with a low supply pressure, $P_s=0.69$ bar (10 psig). In the graphs, the horizontal axis denotes the orbit amplitude (r/c) and data corresponds to two static eccentricities, $e_s = 0$ (centered) and $0.3c$. The results are shown in dimensionless form as $\underline{C}=C/C^*$ and $\underline{M}=M/M^*$. $\underline{C} \sim 1$ and $\underline{M} \sim 1.0$ would show a perfect correlation with the formulas for a fully sealed SFD, Eq. (9). The numerical predictions are derived from the orbit model in Ref. [7] (2016) that reproduces the kinematics of the journal during the experiments.

Note the journal static eccentricity has a small effect on both force coefficients for the PR-SFD. The OR-SFD shows more damping for the off-centered condition ($e_s = 0.3c$). In general, the OR-SFD damping and added mass coefficients increase by $\sim 30\%$ and 20% as the amplitude of whirl motion increases. Note the PR-SFD is less sensitive to changes in both orbit amplitude and off-centered condition. The numerical model predictions are in good agreement with the test data. The large difference between experimental results and ideal predictions, $\underline{C}=1$ with $C^*=12.76$ kNs/m (72.8 lbf.s/in) and $\underline{M}=1$ with $M^*=44$ kg (97 lb_m), demonstrate the limitations of the simple formulas stated in Eq. (9).

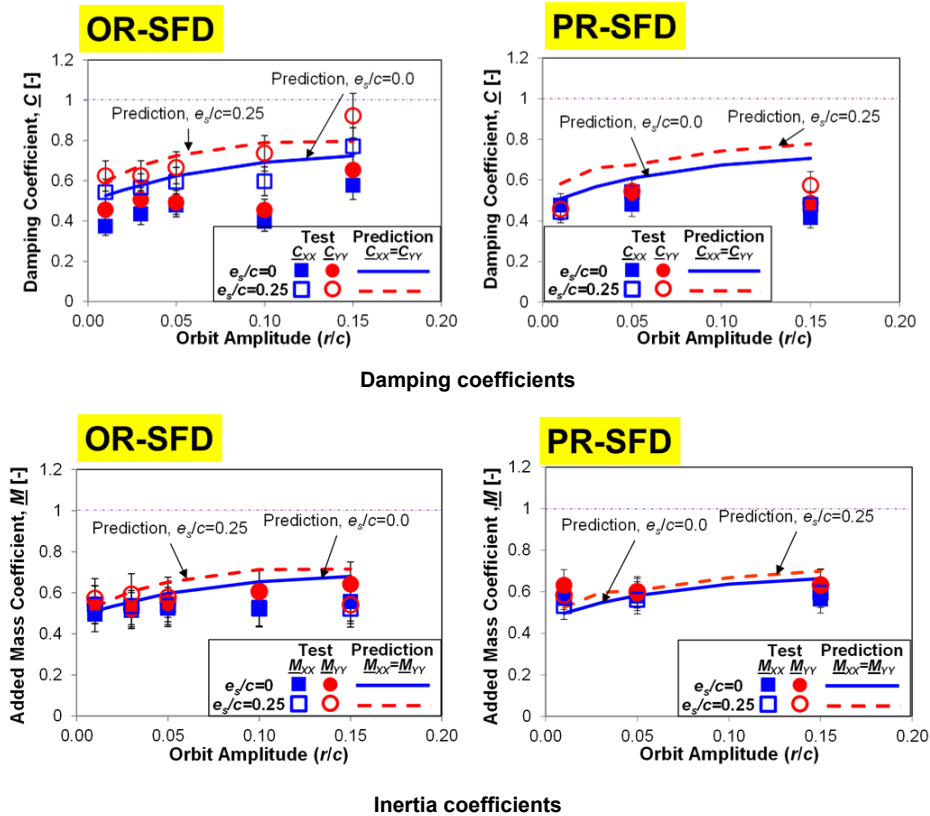


Fig. 22 OR-SFD vs. PR-SFD: dimensionless direct damping ($\underline{C}=C/C^*$) and added mass ($\underline{M}=M/M^*$) force coefficients vs. orbit amplitude and two static positions. Oil supply pressure 0.69 bar(g). Three open feedholes. Taken from Ref. [20] (2019). $C^*=12.76$ kNs/m (72.8 lbr.s/in) and $M^*=44$ kg (97 lb_m)

Effect of number of (open) feedholes on SFD force coefficients

It is of great interest to quantify the performance of SFDs when one or more feedholes clog, hence blocking the passage of fresh lubricant into the squeeze film land region. A mechanical check valve could also fail and stop the oil flow. Figure 23 shows the experimental damping (\underline{C}_{XX} , \underline{C}_{YY}) and added mass (\underline{M}_{XX} , \underline{M}_{YY}) coefficients for both dampers vs. orbit amplitude. Supplied with oil at 0.69 bar (10 psig), the dampers operate with either three feedholes or one feedhole (two holes blocked). In short, the experimental results show that a damper with just one-feedhole generates more damping and added mass coefficients.

At first, the finding may contradict common sense; however, note that feedholes are source of constant pressure and locally distort the dynamic pressure field, hence preventing the generation of squeeze film pressures. The PR-SFD with one feed hole produces less damping than the OR-SFD does, but its added mass coefficient is larger. The OR-SFD with one open feedhole produces 60% more damping than the configuration with three holes. With just one feedhole, $C_{PR-SFD} < C_{OR-SFD}$ and $M_{PR-SFD} < M_{OR-SFD}$ due to air ingestion through the PR slits.

The orbit-model predictions for the three-hole dampers are good. The agreement is lesser for the one-hole dampers that particularly overestimate the damping coefficient. The model underestimates the influence of air ingestion and entrapment. Although the damper ends are sealed, the experimental force coefficients are ~50% of the magnitudes predicted by the theoretical coefficients in Eq. (9), and which do not include either the effect of oil supply pressure, the feed holes, and the leakage through the PR or the oil exit hole in the OR-SFD.

Lessons Learned: OR-SFD vs PR-SFD

- The OR-SFD produces more damping as it avoids air ingestion (to a large extent). O-rings add stiffness and viscoelastic damping to a test system.
- For both PR-SFD and OR-SFD, the larger the number of active feed holes, the lower the damping coefficient. Holes distort and reduce dynamic pressure field, hence the lesser force coefficients.

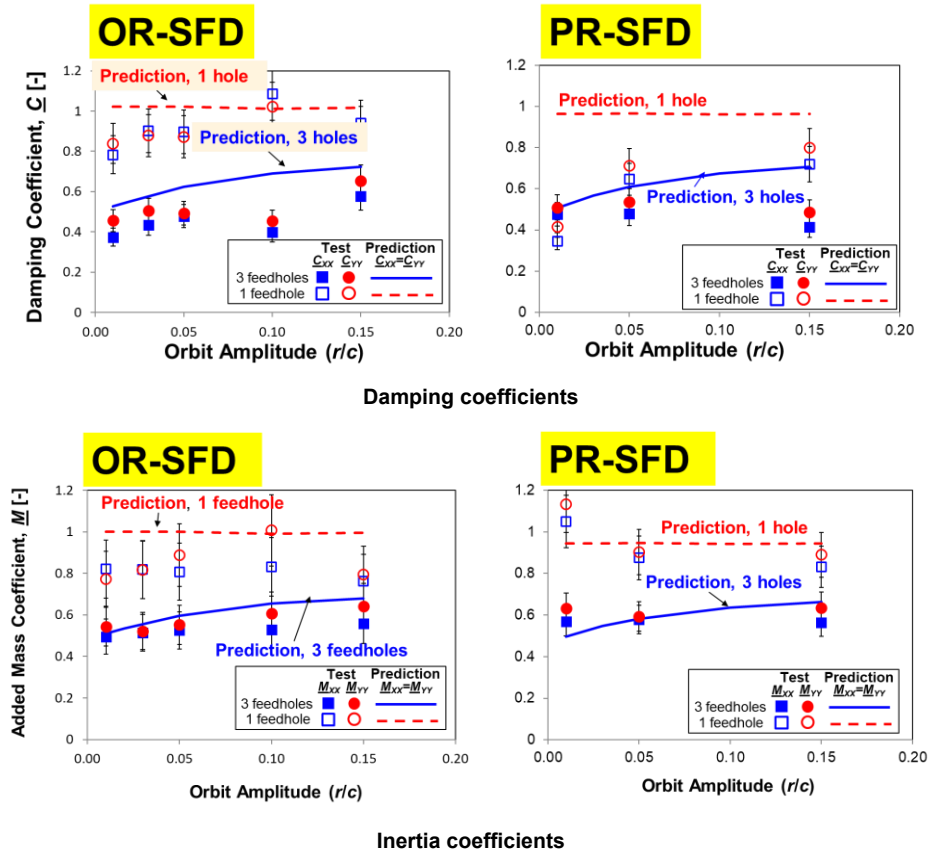


Fig. 23 OR-SFD vs. PR-SFD: three and one feedholes. Dimensionless direct damping ($\underline{C}=C/C^*$) and added mass ($\underline{M}=M/M^*$) coefficients vs. orbit amplitude. Static eccentricity=0 an oil supply pressure 0.69 bar(g). Taken from Ref. [20] (2019). $C^*=12.76$ kNs/m (72.8 lbf.s/in) and $M^*=44$ kg (97 lb_m).

- (c) Damping for OR-SFD increases with static eccentricity (e_s), whereas added mass for OR-SFD and damping and added mass for PR-SFD remain nearly constant.
- (d) Neither the OR-SFD nor the PR-SFD generated cross-coupled force coefficients. That is, $C_{XY}=C_{YX}=0$ and $M_{XY}=M_{YX}=0$
- (e) Film pressures show oil vapor cavitation and persistent air ingestion for operation with a lubricant supplied at a low pressure and for journal motions with a large squeeze velocity (v_s).
- (f) The amount of air entrained in a sealed damper is a function of the squeeze velocity ($>$ threshold) and the pressure supply. Piston rings leak profusely and ingest lots of air. O-rings may appear as a best sealing option; however, they quickly degrade once they lose their compression (squeeze) assembly.

THE INTEGRAL SQUEEZE FILM DAMPER

The basic design of SFDs changed little until the middle 1990's when the wire-EDM processes enabled the construction of integral dampers (ISFDs), see Ref. [21] (TPS 1994). The ISFD, shown in Figure 24, comprises of segmented pads instead of a fully cylindrical journal. Thin structured webs attach the inner and outer rings and perform the function of elastic supports. The thin gap between the pads and the outer ring forms the squeeze film lands. Each pad can be manufactured with a different clearance to counter the static deflection due to rotor weight. Side seals, typically end plates with a tight gap, restrict the axial flow through the film lands, and amplify the damping coefficients by rising the dynamic pressure in a lubricated film undergoing squeeze motions.

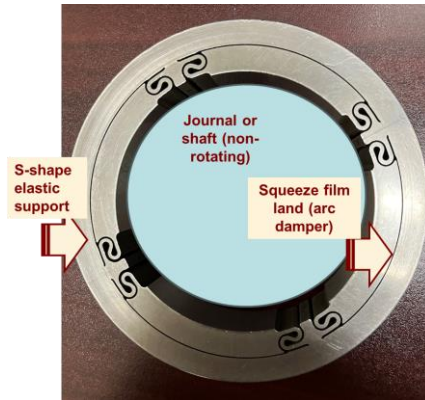


Fig. 24. Photograph of an integral SFD, circa 1997.

ISFDs offer distinct advantages such as reduced overall weight and length of the damper structure with lesser number of parts, accuracy of positioning (centering), and a split segment construction allowing easier assembly, inspection and retrofit than with any other type of damper. Flexure pivot tilting pad bearings offer similar construction features while minimizing (assembly) stack up tolerances and avoiding pivot wear and fretting [21] (1994). The noted advantages are important in aircraft engines where reduced weight and size are a consideration. Unfortunately, to date ISFDs are yet to be applied in jet engines.

Known as a *damper bearing*, the series combination of a flexure pivot tilting pad journal bearing with an ISFD, see Figure 25, has been implemented in numerous compressors to introduce both flexibility and damping to the hydrodynamic bearing. The engineered selection of these two mechanical elements relocates the rotor bearing system critical speeds (rigid modes or first bending mode) well below the mean operating speed and with an optimum damping coefficient at the bearing support. The low structural stiffness of an ISFD and its damping coefficient also isolate the rotor-bearing system from its casing and foundation. For a few applications, please see Zeidan et al. [4] (TPS 1996), and Ertas et al. [22] (2015).

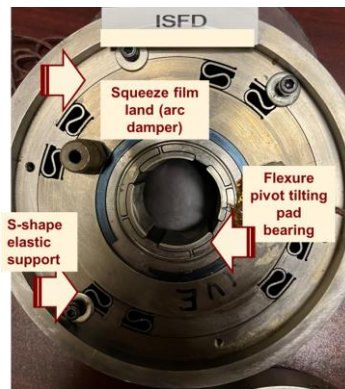


Fig. 25. *Damper bearing*: series integral SFD and flexure pivot tilting pad bearing, circa 2000.

The experimental identification of ISFD force coefficients has lagged their commercial applications⁷. In 2011, Delgado et al. [23] when testing a *damper bearing* found the ISFD generates a significant added mass; a finding largely ignored by manufacturers' specifications to the current date (2025). Similarly, in 2012 Agnew and Childs [24] tested a *damper bearing* and report the series element produces stiffnesses and damping force coefficients that are roughly ~ 50% of the force coefficients for the tilting pad bearing alone. The tilting pad bearing force coefficients were extracted after locking the ISFD (inactive damper). The reduction in K , C as shaft speed increases is the expected outcome. Ref. [24] also reports added mass coefficients ~ 20 kg (44 lb_m) for the *damper bearing*, and 20 to 40 kg (88 lb_m) for the flexure pivot journal bearing alone. Contrary to a commonly held assumption, the series journal bearing-ISFD produces less damping, not more.

Recently, dedicated test campaigns have produced force coefficients (K , C , M) for ISFDs with the intention of furthering their

⁷ Suggestion: watch the video clip from a bearing manufacturer: <https://www.youtube.com/watch?v=HIXZNOYFbXk>

adoption in upcoming high-speed, compact turbomachinery processing CO₂ for carbon capture and sequestration, H₂ transport, and in waste heat generation. See Refs. [25] (2018) and [26] (2024).

Effect of end seals gap or clearance on ISFD force coefficients

Figure 26 shows photographs of the *damper bearing* tested by Agnew and Childs [24] (2012). The series mechanical element was designed for application to a hydrocarbon gas compressor. In 2021, see Ref. [27], the flexure pivot bearing was shimmed (inactive) for identification of the ISFD force coefficients. Table 3 lists the ISFD geometry, lubricant, and operating conditions. Figure 27 shows a drawing of the ISFD and a schematic cross section of the side plates making the end seals.

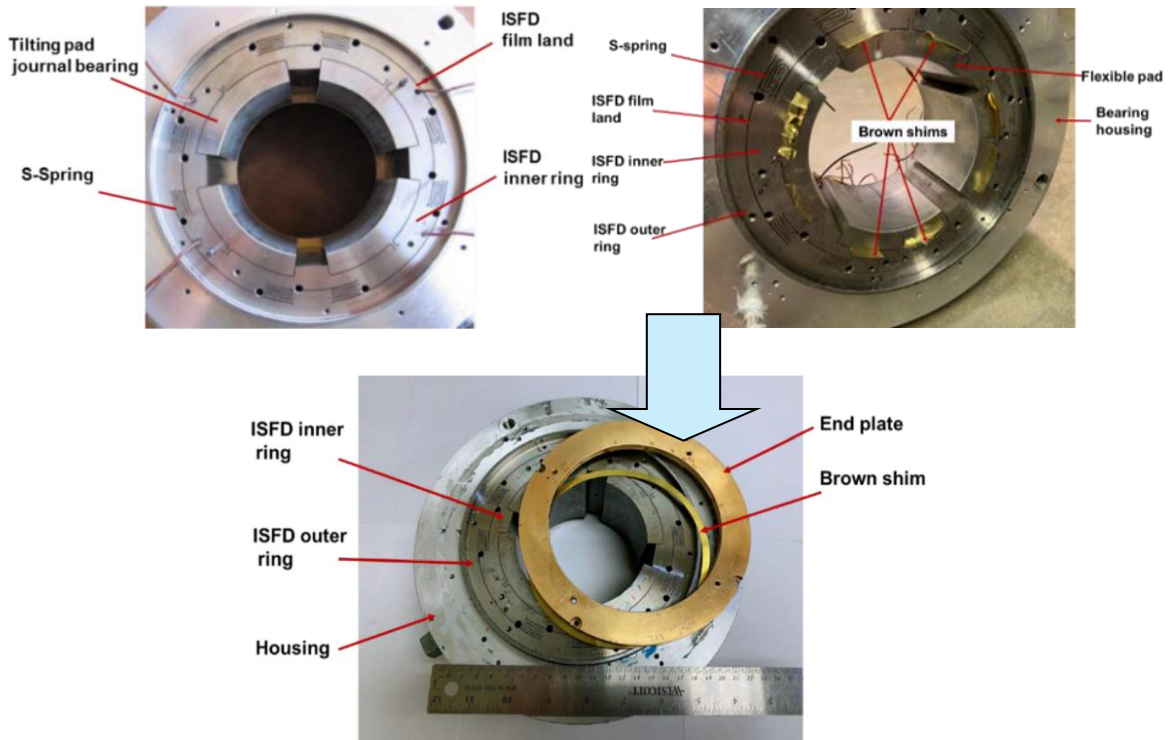


Fig. 26 Top: Photographs of test ISFD-TPJB [24] and shimmed hydrodynamic inner film for tests with SFD alone [27].

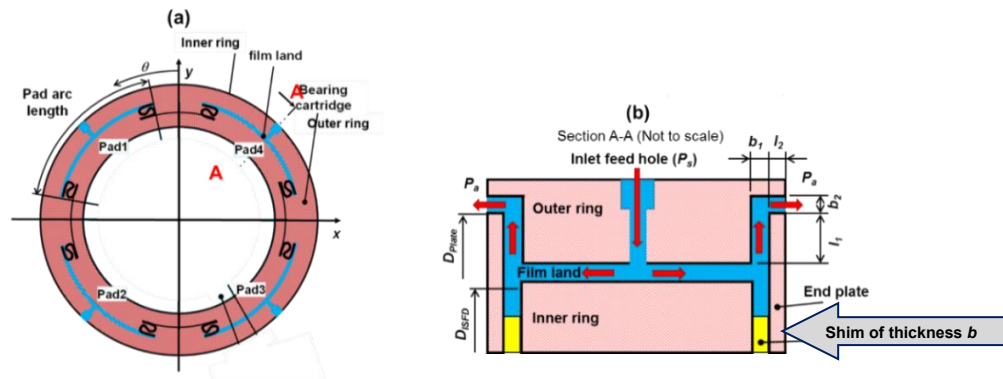


Fig. 27 Front and cross section views of test ISFD. Lubricant flow path and nomenclature for end plate seals shown (not to scale).

Table 3. Test ISFD dimensions and operating conditions. Taken from Ref. [27].

Geometry	SI unit	US unit	ISO VG 46 46 °C (115 F)	SI unit	US unit
Land length, L	76 mm	3 inch	Viscosity, μ	31.2 cPoise	4.5 10^{-6} psi.s
Diameter, D	157 mm	6.22 inch	Density, ρ	860 kg/m ³	53.7 lb/ft ³
Radial clearance, c	0.356 mm	14 mil	$\nu = \mu/\rho$	3.63 10^{-5} m ² /s	56 10^{-3} in ² /s
Number of films	4		Feed orifice	1.93 mm	5/64 inch
Arc length	73°				
End seal length, l_1	7.75 mm	1/3 inch	Gap b_1	0.28, 0.43 mm 0.53 mm	0.79 c , 1.21 c 1.49 c
Whirl frequency, ω	9-166 Hz		Pressure, P_s	1 - 2 bar	15-30 psig
Motion amplitude, r	0.05 c		Flow, Q_{oil}	9.5 liter/min	2.5 GPM
Squeeze velocity, v_s	18.5 mm/s	0.73 in/s	Reynolds#	Max. 3.64	
			Re_s		

The experimental campaign quantified the ISFD force coefficients as a function of the static eccentricity (e_s) and the gap (b_1) configured in the end plate seals. For reference, the elastic structure stiffness $K_S \sim 60$ MN/m (343 klbf/in), and the mass of the housing and ISFD $M_{BC} = 19$ kg (42 lbf). Applied between two pads, a static load ~ 15 kN (3,360 lbf) displaced the damper journal to a static eccentricity as large as $e_s = 0.7c$. For identification of the ISFD force coefficients, pseudo random generated dynamic loads covered a frequency range from 9 to 166 Hz, in steps of ~ 10 Hz, and produced bearing motions of small amplitude, $\sim 5\%$ of the ISFD clearance.

Figures 28 and 29 display the experimental damping (C_{XX}, C_{YY})_{ISFD} and added mass (M_{XX}, M_{YY})_{ISFD} coefficients vs. static eccentricity (e_s) and several end seal gaps, b_1 . The parameters⁸ shown are *true* rotordynamic coefficients since they correspond to small amplitude motions around e_s . Both damping and inertia coefficients modestly grow as e_s increases; and most importantly, when compared to the open ends condition, note the significant increase in damping and inertia coefficients as the gap (b_1) of the end plate seals reduces.

The tightest end seal gap of 0.28 mm (11 mil), $b_1/c = 0.78$, severely restricts the axial flow, and the ISFD generates quite large damping coefficients, approximately 22 times more than the coefficient estimated for the open ends ISFD (no end plates installed). Similarly, the added mass coefficients are large, ~ 50 kg (110 lbf) for the ISFD with an end seal gap = 0.53 mm (21 mil), $b_1/c = 1.5$. Hence, tightly sealed ISFDs produce significant magnitude damping (and added mass) coefficients.

Simple formulas for estimating the damping (C) and added mass (M) coefficient of an ISFD are:

$$(C_{XX} = C_{YY})_{openISFD} = \frac{1}{2} \pi \mu \frac{DL^3}{c^3} \left(\frac{Pad_{arc}}{90^\circ} \right); (M_{XX} = M_{YY})_{openISFD} = \frac{1}{24} \pi \rho \frac{DL^3}{c} \left(\frac{Pad_{arc}}{90^\circ} \right) \quad (21a)$$

$$(C_{XX} = C_{YY})_{sealedISFD} = \frac{12}{8} \pi \mu \frac{LD^3}{c^3} \left(\frac{Pad_{arc}}{90^\circ} \right)^3; (M_{XX} = M_{YY})_{sealedISFD} = \frac{1}{8} \pi \rho \frac{LD^3}{c} \left(\frac{Pad_{arc}}{90^\circ} \right)^3 \quad (21b)$$

Above, the pad arc is in degrees. Note the ratio of force coefficients sealed/open ends = $3 (D/L \times Pad_{arc}/90^\circ)^2$. The formulas, apply to small amplitude journal motions around the centered position ($e_s = 0$). The simple equations do not account for either feed holes or the magnitude of supply pressure or the flow resistance of the end (plate) seals.

A commercial bearing manufacturer [28] publishes guidelines for the selection of a stiffness for the ISFD and states its damping coefficient equals

$$C_{ISFDw} = \left(\frac{1}{48} \text{ to } 1 \right) \frac{12}{8} \pi \mu \frac{LD^3}{c^3} \quad (22)$$

The manufacturer argues the “*ISFD design prevents circumferential flow and controls damping by flow resistance at the oil supply nozzle. It absorbs energy more like a shock absorber*”. However, the formula above shows neither the size of a feed orifice nor the arc length of the squeeze film lands. The formula reveals the damping coefficient varies up to 48 times from its low

⁸ As per Ref. [27], the experimental uncertainty varies from 2% to 5% of the identified coefficient. Error bars, denoting mainly the variability from frequency averaging of multiple tests, appear very small in the graphs.

magnitude to its high magnitude. Incidentally, the manufacturer does not mention any added mass effect.

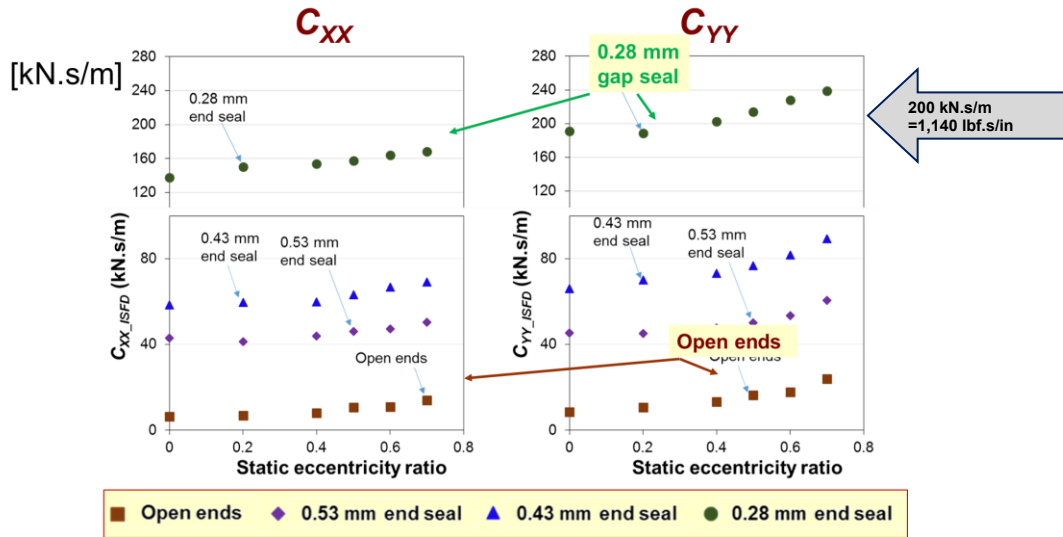


Fig. 28 ISFD experimental damping coefficients vs. static eccentricity ratio (e_s/c) and several gaps for the end seals. Clearance $c=0.356$ mm (14 mil). Taken from Ref. [27]. Note $200 \text{ kN.s/m} = 1.14 \cdot 10^3 \text{ lbf.s/in}$.

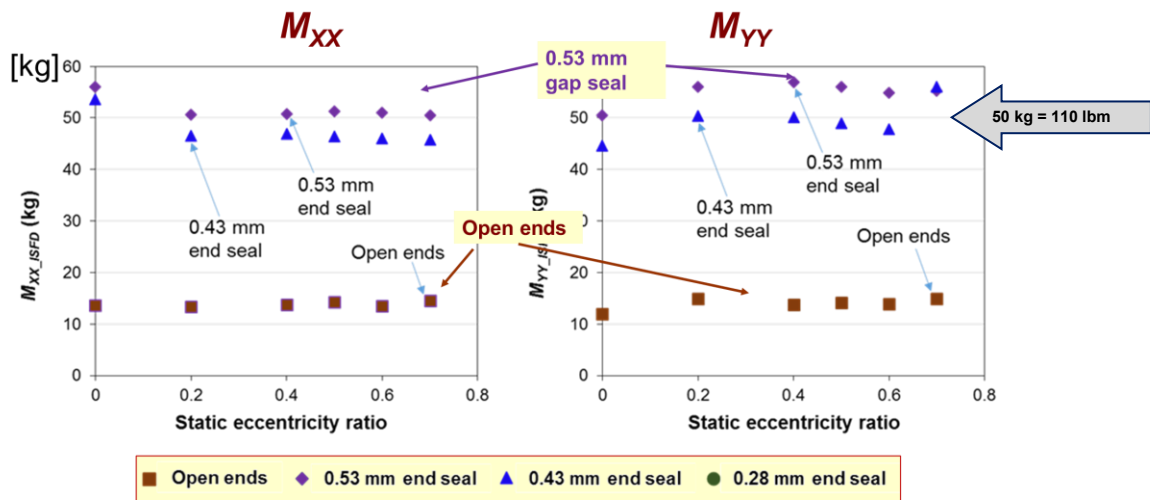


Fig. 29 ISFD experimental added mass coefficients vs. static eccentricity ratio (e_s/c) and several gaps for the end seals. Clearance $c=0.356$ mm (14 mil). Taken from Ref. [27]. Note $50 \text{ kg} = 110 \text{ lbm}$.

Reproduced from Ref. [27], Figures 30 and 31 show predicted and experimental force coefficients vs. the static eccentricity ratio (e_s/c). For simplicity, the data shown is the arithmetic average of the force coefficients along the two directions, i.e., $C_{ISFD} = \frac{1}{2}(C_{XX} + C_{YY})$. Be mindful about the distinctly small vertical scale for the results obtained for the open ends ISFD. In general, the numerical model [27] predicts well the damping coefficients for motions about the centered condition, $e_s=0$. The discrepancy between prediction and measurement increases as the static eccentricity increases. Most important, however, is to realize that the experimental results do not reveal a strong non-linearity as the predictions otherwise show.

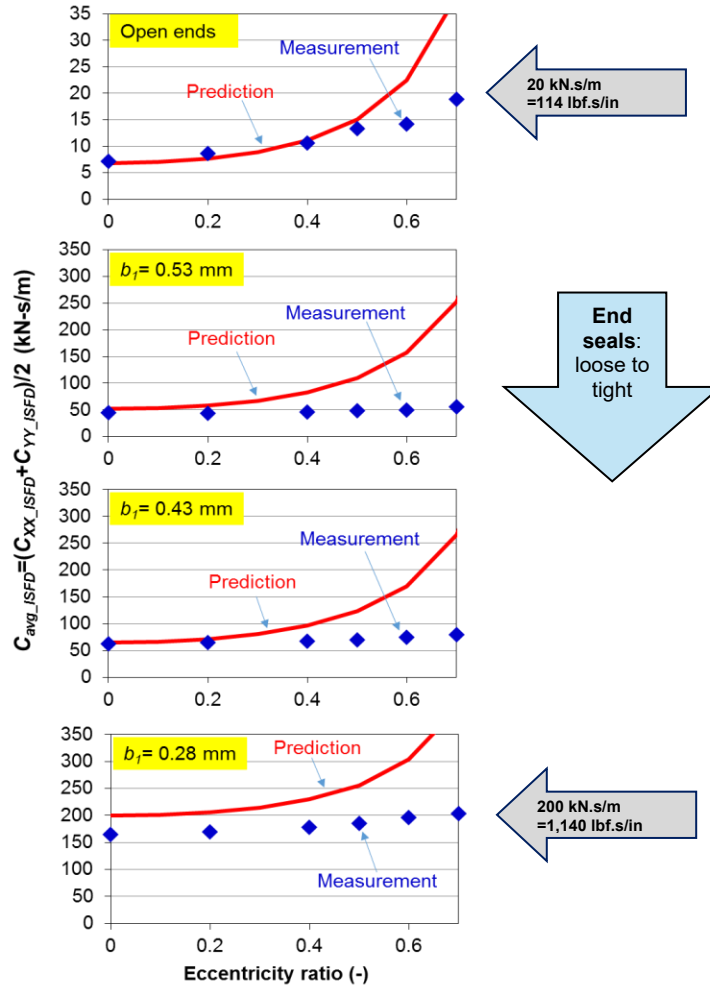


Fig. 30 ISFD damping coefficients (C_{ISFD}) vs. static eccentricity ratio (e_s/c): predictions and experimental results. Open ends ISFD and sealed ends ISFD with gap $b_1=0.53$ mm, 0.43 mm, and 0.28 mm ($=0.78$ c) and clearance $c=0.353$ mm.

Figure 31 depicts the predicted and experimental added mass coefficients ($M_{ISFD} = \frac{1}{2}(M_{XX} + M_{YY})$) vs. static eccentricity (e_s/c). The experimental M_{ISFD} are at least 2.5 times larger than the predicted magnitudes. That is, the model largely under-predicts the added mass coefficients. As a side note, realize that Delgado et al. [23] (2011) found, when testing an ISFD, an added mass coefficient that is one order of magnitude larger than the predicted magnitude. On the other hand, Ertas et al. [25] (2018) report virtual mass coefficients significantly smaller than predictions.

Worthy of note, the tests with the tightest end seal ($b_1/c = 0.78$) produced an unexpected stiffening of the test bearing, i.e., a negative added mass. The unusual effect is due to the compressibility of the lubricant having a small amount of dissolved gas. In a ISFD with very tight end seals, the lubricant cannot easily displace either axially or circumferentially, hence the squeeze film action generates a dynamic pressure field that compresses the lubricant to produce the hardening effect.

Figure 32 shows predictions of the ISFD damping and added mass coefficients vs. the end seals gap (b_1) and small amplitude motions about the centered position ($e_s=0$). The figures include the experimental force coefficients obtained for gaps $b_1=0.28$, 0.43 and 0.53 mm. Note the rapid increase of the force coefficients as the end gap decreases, from open ends to tightly sealed ends (no through flow). It is important to realize the fully sealed condition is not physically possible as the trapped lubricant would force the damper to lock, hence not allowing for any journal displacement.

The ISFD force coefficients shown, experimental and predicted, are derived from (infinitesimally) small amplitude motions about a static condition. Hence, they are *true* rotordynamic force coefficients as per the classical definition [7]. A damper performing very small amplitude motions will show neither oil cavitation (vapor or gas) nor ingest air into the film. However, when a damper undergoes sizeable amplitude dynamic displacements, a large squeeze velocity (v_s) will not just generate the squeeze film pressure field but also drive the lubricant to cavitate and/or draw in air into the film. See Figure 19 and Appendix B for further details.

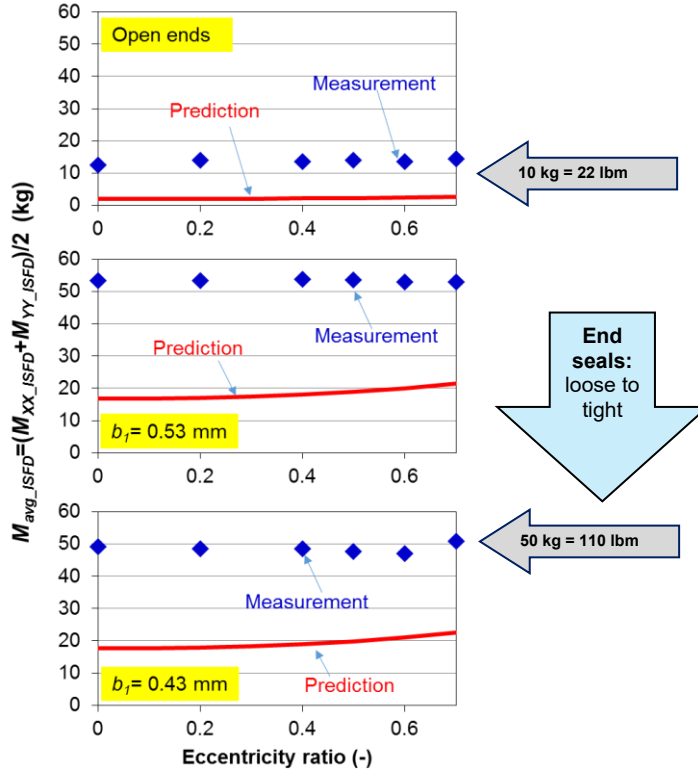


Fig. 31 ISFD added mass coefficients (M) vs. static eccentricity ratio (e_s/c): predictions and experimental results. Open ends ISFD and sealed ends ISFD with gap $b_1=0.53$ mm and 0.43 mm ($=1.2 c$) and clearance $c=0.353$ mm (14 mil).

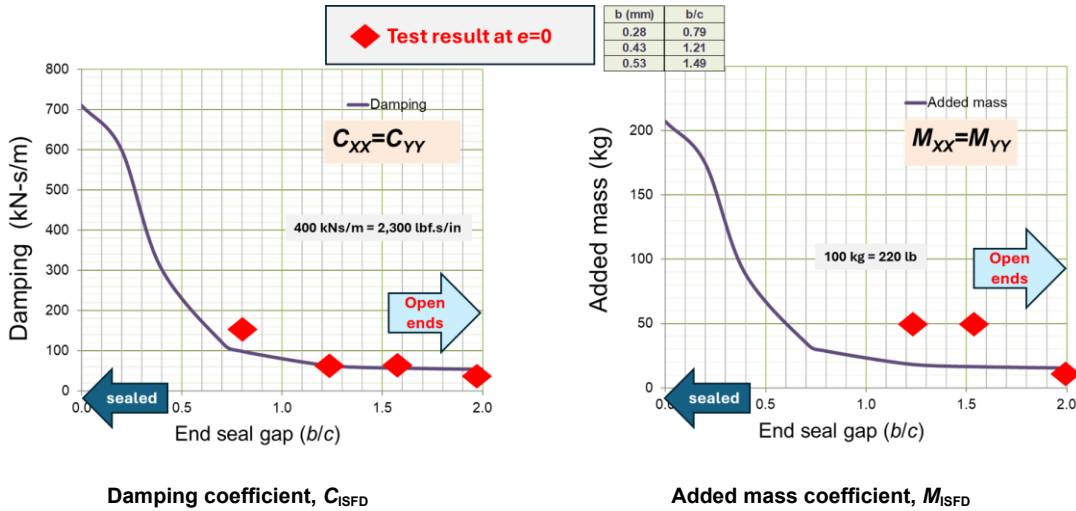


Fig. 32 Predicted ISFD force coefficients (C, M) vs. gap (b_1/c). Centered condition ($e=0$). ISFD clearance $c=0.353$ mm (14 mil). Experimental results \blacklozenge from Ref. [27] included.

For the test ISFD configuration with end seal gap $b_1=0.43$ mm ($1.21 c$), Figure 33 shows the force coefficients vs. squeeze film velocity ($v_s = r\omega$) for a journal describing circular centered motions with amplitude (r) and at two whirl frequencies $\omega = 50$ and 100 Hz. The oil supply pressure $P_s = 1.5$ bar (23.8 psig) is rather low. For $v_s = 50$ mm/s (2 in/s), the orbit size $r = 0.45c$ and $0.225c$ at the low and high whirl frequencies, 50 and 100 Hz respectively. Below the damping and added mass coefficients are obtained from the (period averaged) tangential and radial forces as $C = -F_t/V_t$ and $M = -F_r/A_r$, see Eq. (6). Recall the journal tangential velocity and radial acceleration are $V_t = v_s = (r\omega)$ and $A_r = (-r\omega^2)$. The predicted damping and added mass coefficients rapidly reduce as v_s increases because the oil cavitation zone increases. Hence, for practical purposes do not rely on a damping

specification obtained from either predictions or measurements obtained from small amplitude motions ($v_s \rightarrow 0$).

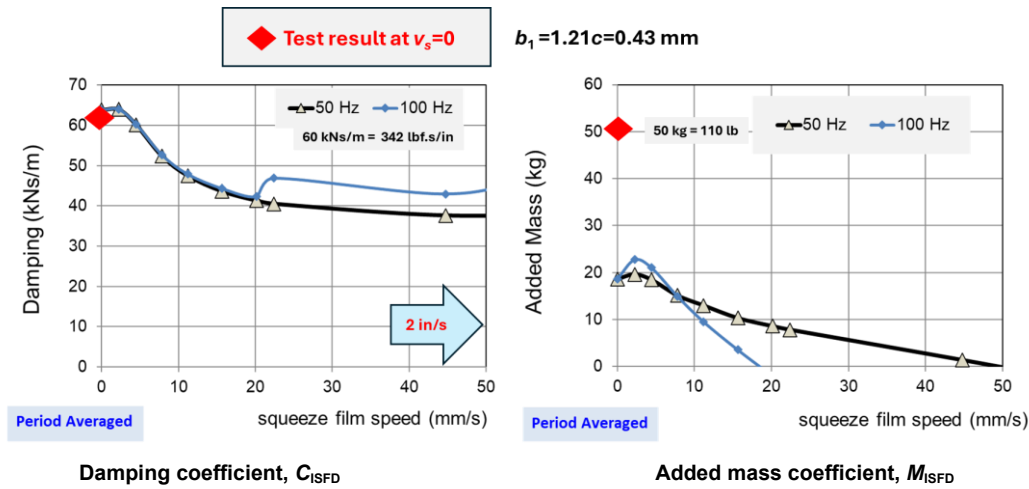


Fig. 34 Predicted ISFD damping and inertia force coefficients (C, M) vs. squeeze film velocity. Circular centered motions at two whirl frequencies. ISFD clearance $c=0.353 \text{ mm}$ (14 mil) and seal end gap $b_1 = 1.21c$. Experimental results included.

THE LEARNING TO DATE

Decades of practice demonstrate that squeeze film dampers generate damping even when operating with persistent air entrainment. Dampers also produce significant added mass coefficients, often larger than the journal mass. A soft structural stiffness of the damper support (squirrel cage or flexures) allows the journal to displace, and the damper generates a reaction force that dissipates mechanical energy. Due to persistent air ingestion, the damping coefficient decreases for operation with large squeeze film velocities (= amplitude of motion x whirl frequency). The reduction in damping at high frequencies and large motion amplitudes is beneficial in rotor-bearing systems operating away from critical speeds.

Childs [2] (2012) notes that because of lubricant cavitation and unquantifiable air ingestion, correlation between theory and experiment is less compelling for SFDs than for journal bearings. Today, modern predictive models, accounting for fluid inertia, feed grooves and holes, air ingestion and entrapment, and end seals produce damper forces in agreement with the experimental record. Overly simplistic models based on classical lubrication do poorly. The idealized geometry models predict damper force coefficients which are highly nonlinear, varying greatly with the static eccentricity or the orbit amplitude. The experimental record demonstrates that SFDs and ISFDs are quite linear mechanical elements; that is, both the motion amplitude and static off-centering influence little the magnitude of the damping and inertia force coefficients.

In the design of stable rotordynamic systems, damping is the critical design consideration. If damping is too large, a SFD acts as a rigid constraint to the rotor-bearing system with large forces transmitted to the support structure. If damping is too light, the damper is ineffective and would permit excessively large amplitudes of rotor motion, often subsynchronous. In actuality, the physical magnitude of the damping coefficient is irrelevant; rather the viscous damping ratio for the whole system is important. Hence, SFDs are to be designed and implemented with full knowledge of the rotor-bearing system, namely modal stiffnesses and masses that define the system natural frequencies and the modal damping ratios. Hence, to be effective, a damping element must be "soft" to allow for motions (or displacements) at the location of the support when crossing natural vibratory modes (traversing critical speeds). As a cautionary note, dampers designed with overly tight end seals could produce damper lock-up due to their sizeable viscous damping. The lubricant, confined into a fixed volume, has no route for ready evacuation. In sum, the SFD and its support stiffness must be tailored to the rotor-bearing system to engineer the placement of critical speeds, to reduce the amplitude of whirl motions, and to enhance rotordynamic stability. That is, both viscous damping and support stiffness must be considered in the design of an SFD for a rotor bearing system.

Although ISFDs have been around for ~ 30 years, their application is still limited to certain types of centrifugal compressors; often in the aftermarket as a drop-in retrofit. Their major role is to displace system critical speeds away from the mean operating speed. In this last case, ISFDs offer also structural isolation. Despite their significant advantages, the use of ISFDs in aircraft engines has not taken place. Their time is ripe, as air breathing engine manufacturers search for ultra-short damper configurations ($L/D < 0.2$). The savings in axial space will shorten overly long, multiple shaft flexible rotors. Combined flexure-pivot hydrodynamic bearings in series with ISFDs are quite promising for the novel application of Carbon capture and sequestration, waste heat generation, and the upcoming Hydrogen processing turbomachinery.

NOMENCLATURE

A_X, A_Y	Components of journal center acceleration [m/s ²]	M_J	$(\frac{1}{4} \rho_{steel} \pi D^2 L)$. Mass of steel journal [kg]
A_r	$-r\omega^2$. Journal center radial acceleration	P	Pressure field [Pa]
b	End plate seal axial gap [m]	P_s, P_a	Oil supply pressure and ambient pressure [Pa]
c	Film radial clearance [m]	$\dot{\varphi}$	Viscous dissipated power [W], $C_{it} v_s^2$ for CCO.
$C, C_{\alpha\beta}$	Damping coefficients, X, Y & r, t [Ns/m], $C=C/C^*$	Q_{oil}	Supplied lubricant flow [m ³ /s].
C^*	$12\pi\mu L(D/2c)^3$. Fully sealed damping coeff [Ns/m]	q_{end}	$\frac{1}{2} Q_{oil}/(\pi D)$. Flow per unit length through one end [m ² /s].
C_{crit}	$2(K_e/\omega_n)$. System critical damping [Ns/m]	(r, t)	Radial and tangential (whirl) coordinates.
C_{seal}	$1/R_{seal}$. Empirical end seal coefficient [(m ² /s)/Pa]	r	Amplitude of orbital motion [m], $r=r/c$
D	$D=2R$. Journal diameter [m]	Re_s	$(\rho/\mu)\omega c^2$. Squeeze film Reynolds number
e_s	Journal static eccentricity [m]. $\varepsilon_s = e_s/c$	V_X, V_Y	Components of journal center velocity [m/s]
(e_X, e_Y)	Components of journal center displacement [m]	V_t	Journal center tangential velocity [m/s]
(F_X, F_Y)	Components of SFD reaction force [N]	v_s	$r\omega$. Squeeze film velocity [m/s]
f_n	$2\pi \omega_n$. Natural frequency (Hz)	(X, Y)	Coordinate system on plane of bearing [m]
h	Film thickness [m]	z	Axial coordinate [m]
$H_{\alpha\beta}$	System complex dynamic stiffnesses [N/m]	β	Gas volume fraction, GVF [-]
i	Imaginary unit	ΔP	$(P_{end}-P_a)$. Pressure drop across end seal [Pa]
K_e	Modal stiffness [N/m]	ζ	C/C_{crit} . Damping ratio [-]
$K, K_{\alpha\beta}$	Static stiffnesses, $\alpha\beta=X, Y$ & r, t [N/m]	γ	$Q_{oil}/(\pi L D v_s)$. Squeeze-flow parameter for CCO.
K_s	Structure static stiffness [N/m]	μ, ρ	Oil viscosity [Pa.s] and density [kg/m ³]
L	Damper axial length [mm]	θ	circumferential coordinate [-]
l	End seal length [m]	ω	Excitation frequency [rad/s]
M_e	System (modal) mass [kg]	ω_n	Natural frequency [rad/s]
$M, M_{\alpha\beta}$	Added mass coefficient, $\alpha\beta=X, Y$ & r, t [kg], $\underline{M}=M/M^*$	Abbreviations	
M^*	$\rho\pi(L/c)(\frac{1}{2}D)^3$. Fully sealed added mass coeff [kg]	CCO	Circular centered orbit
M_{BC}	Mass of bearing and support structure [kg]	SFD	Squeeze film damper
M_o	$(\rho \pi D L c)$. Mass of fluid in squeeze film [kg]	ISFD	Integral squeeze film damper
		OR-SFD	SFD sealed with O-rings
		PR-SFD	SFD sealed with piston rings (PR)

APPENDIX A. Examples of air ingestion and entrapment: pressure profiles and photographs of oil condition

Meticulous experimentation⁹ demonstrates that persistent air ingestion and entrapment degrade the forced response of open ends SFDs, see Ref. [16] (2001) for example. A simple criterion gives the likelihood of air ingestion with the feed-squeeze flow parameter (γ) that relates the lubricant supplied flow rate (Q_{oil}) to the dynamic change in volume in the film, i.e.

$$\gamma = Q_{oil}/(\pi L D v_s) \quad (A.1)$$

where $v_s = (r\omega)$ is the squeeze velocity. When $\gamma > 1$ no air entrainment occurs, i.e., the through flow is sufficient to fill the volume change caused by the journal circular whirl motion. On the other hand, air ingestion and entrapment occur when $\gamma < 1$. The lower the feed-squeeze parameter (γ), the more severe the reduction in damper reaction forces. Ultimately, operation at large v_s increases air ingestion, prevents oil vapor cavitation, and reduced considerably the forces available from the SFD.

As a relevant example, Fig. A1 displays graphs for three periods of pressure waves recorded at the midplane of a PR-SFD and at two angular locations, 225° and 315°. For reference, the oil supply pressure (P_s) increases from low (top graph) to high (bottom graph). The damper describes circular centered orbits with amplitude $e=0.65 c$ at a frequency of $\omega=60$ Hz; hence, $V_t=e\omega=60$ mm/s. For the same P_s , note the significant differences in film pressure waves at the two angular locations although the journal

⁹ The National Science Foundation (NSF) and the Texas A&M University Turbomachinery Research Consortium (TRC) supported the fundamental research work quantifying SFD fluid flows.

kinematics process is identical. Both peak-peak pressures differ, and they are not out of phase by 90° as the journal motion would dictate for an idealized damper (no holes or sinks). That is, the location of the feedhole and the PR slits affects the pressure waves. Note that the magnitude, peak-peak, of the film pressures increases as the supply pressure increases. At the lowest $P_S=0.69$ bar(g), oil vapor cavitation appears, and air ingestion is small since film pressures are also small. At the intermediate pressure $P_S=2.8$ bar(g), the film peak-to-peak pressures are larger, and with a persistent air ingestion, produce noisy pressure waves with sudden pressure bursts (high frequency) that make the gas bubbles collapse. The highest $P_S=6.9$ bar(g) is large enough to prevent either air ingestion or lubricant vaporization. Hence, as shown in the prior figures, the PR-SFD will produce force coefficients increasing in magnitude as the supply pressure P_S grows from lowest to highest.

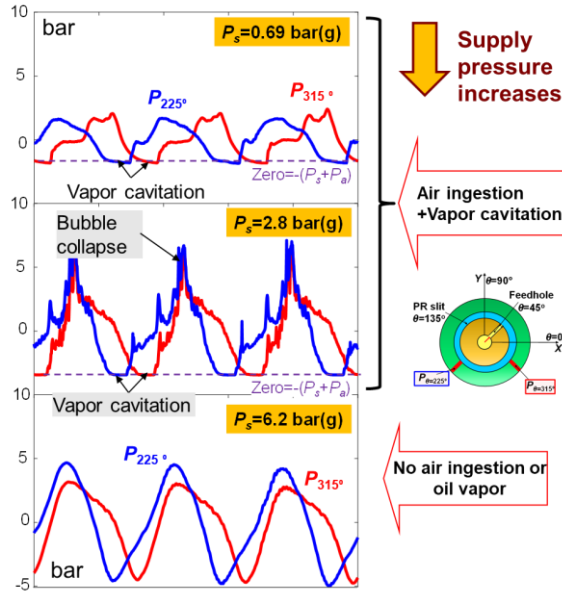


Fig. A1 PR-SFD: Measured dynamic film pressure waves at two angular locations vs. magnitude of oil supply pressure, 0.69 to 6.2 bar(g). Circular centered orbits with amplitude $e=0.65c$ and frequency 60 Hz. One feedhole. Squeeze film speed $V_t = 90$ mm/s and squeeze film Reynolds # $Re_s = 15.52$. Taken from Ref. [20] (2019).

Figure A2 shows photographs of the oil exiting the PR-SFD for two oil supply pressures. The journal kinematics are the same as those in Fig. A1. For the low P_S , the oil bubbles through the PR slit to make a foamy mixture. For the high P_S , liquid jets out through the PR slit and the lubricant accumulating on the exit side shows less bubble. The larger supplied flow rate (at the higher P_S) prevents the ingestion of air into the squeeze film, as shown in Fig. A1 (bottom graph).

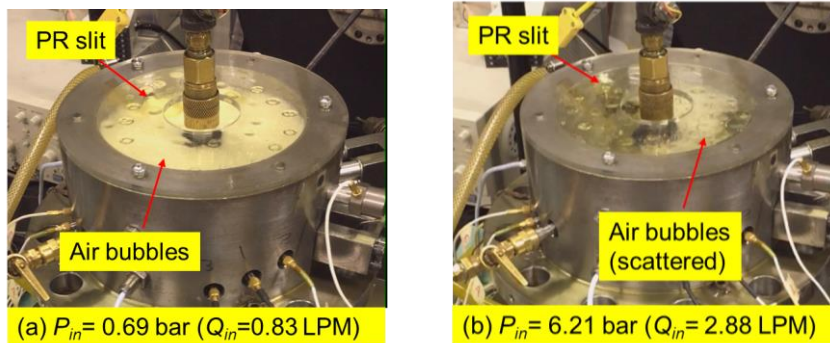


Fig. A2 PR-SFD: Photographs of lubricant exiting on the top side. (a) $P_S=0.69$ bar(g) ($Q_{in}=0.83$ LPM) and (b) $P_S=6.21$ bar(g) ($Q_{in}=2.88$ LPM). Circular centered orbit with frequency 60 Hz and orbit radius $e=0.65c$. One lubricant feedhole. Taken from Ref. [24] (2019).

Similarly, Figure A3 depicts photographs of the time evolution of the lubricant exiting the PR-SFD and its accumulation on the top side. Note the major differences for operation at two pressures, one low and one moderately high. For the low P_S , there is

more air ingestion that, as time progresses, makes a foamy mixture. The photographs show the PR cannot fully seal the lubricant flow as there is persistent leakage through the PR slits.

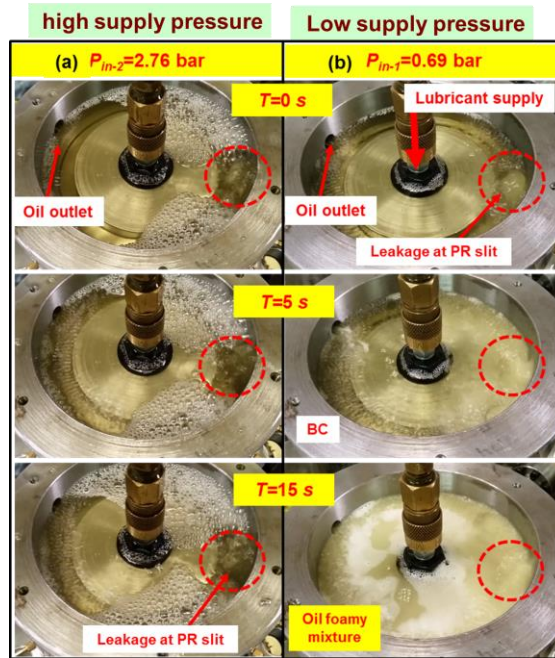


Fig. A3 PR-SFD: Photographs of evolution of lubricant exiting on top side of damper. (a) $P_s=2.76$ bar(g) and (b) $P_s=0.69$ bar(g) bar ($Q_{in}=2.88$ LPM). Taken from Ref. [20] (2019).

Table A1 lists the URLs for several short videos recorded during the experiments. The videos make palpable the persistence of air ingestion and entrapment on the operation of dampers (open ends, piston rings sealed, or with O-ring seals) and under large enough squeeze film velocities. In general, increasing the lubricant supply pressure to avoid or to ameliorate the detrimental effect of air entrapment in a SFD is not practical for aircraft jet engines. The demand of a high-pressure pump more and larger volume for oil storage are not options in an application where weight and volume are at a premium.

The last video shows a record of the simple hands-on method to quickly quantify the entrained gas volume fraction (GVF) while the damper is in operation. The simple procedure can readily assist the validation of computational models and their ability to predict accurate force coefficients.

Table A1. Universal record locators (URLs) for video clips of SFD performance and oil exit condition

URL	Short description	Reference
https://www.youtube.com/watch?v=Tqceie9mbdE	SFD test rig overview at Rotordynamics Laboratory	(2020) Texas A&M University
http://youtu.be/8wQ1TnGTmyE http://youtu.be/6xNra8umKEw	Open SFD – Condition of lubricant exiting to top side and bottom side. $L = 25.4$ mm, $c = 0.025$ mm, $P_s = 0.41$ bar(g), flow: 5.0 liter/min	(2014) Texas A&M University
https://www.youtube.com/watch?v=PulQisPDRtY	PR-SFD: Time Evolution of lubricant condition through top exit section. Two supply pressures	Ref. [20] (2019)
https://youtu.be/R5WPD6t1fWs	OR-SFD: Lubricant flow exit condition for increasing squeeze velocities	Ref. [19] (2024)
https://youtu.be/AtVBw5XMdcw	OR-SFD: Measurements to estimate the GVF from experiments with orbit amplitude $r = 0.15c$ to $0.45c$ and whirl frequency $\omega = 55$ Hz and 70 Hz.	Ref. [19] (2024)

APPENDIX B. Description of SFD test rig and procedure for identification of force coefficients

This section describes a test rig constructed to quantify the performance of ultra-short length SFDs with end seals. The configurations are directly applicable to aircraft engines. Refs. [6] (2016), [20] (2019), [19] (2024) detail the measurements and parameter identification, the identified force coefficients from small and large amplitude whirl motions over a wide frequency range, and comparisons to physical model predictions.

Figure B1 depicts the SFD test rig comprising a rigid pedestal, four support rods, a journal, and a bearing cartridge (BC). Two orthogonally placed electromagnetic shakers and stingers apply dynamic loads to the BC and produce circular or elliptic orbits, centered or off-center. Installed in the BC, along the X and Y axes, pairs of accelerometers, eddy current sensors, and load cells measure the BC accelerations, the displacements relative to the fixed journal, and the applied shaker loads.

Figure B2 shows top and cross-section views of the BC and journal with end grooves for installation of O-rings (ORs). The squeeze film section is short in axial length, $L = 25.4$ mm (1 inch), and the journal diameter $D = 127$ mm (5 inch), ($L/D=0.2$). The film radial clearance $c = 0.373$ mm (15 mil), ($D/c=341$), although dampers with other various clearances were constructed.

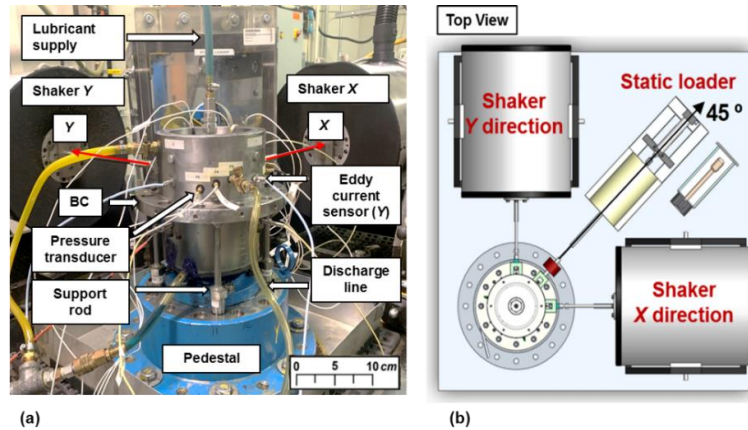


Fig. B1 (a) Photograph and (b) schematic top view of SFD test rig with electromagnetic shakers and static loader.

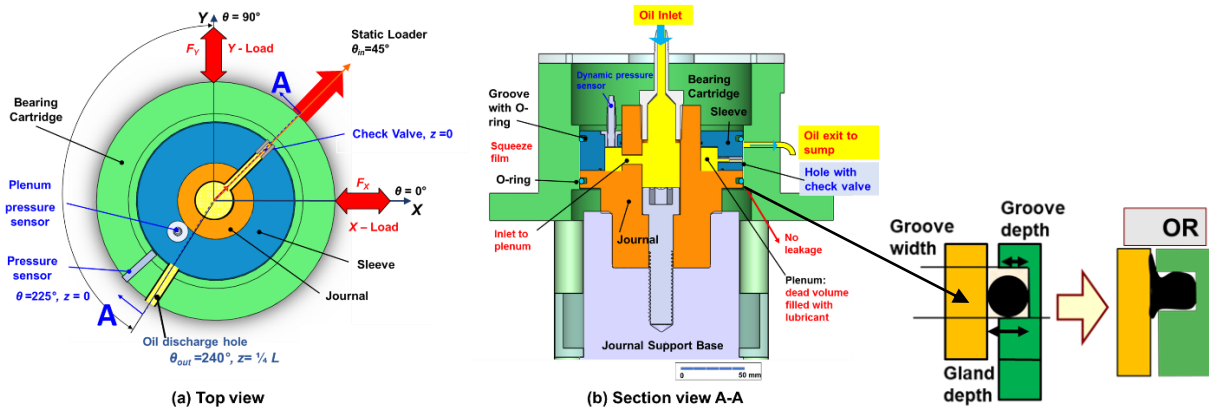


Fig. B2 OR-SFD (a) top view featuring one lubricant feedhole ($\theta_{in} = 45^\circ$, $z = 0$) and a discharge hole ($\theta_{out} = 240^\circ$, $z = +\frac{1}{4}L$); and (b) section A-A showing installed ORs. (Drawings not to scale and with exaggerated features). From Ref. [26].

A pump supplies ISO VG 2 lubricant at pressure P_s , ranging from low=0.69 bar(g) (10 psig) to high=6.9 bar(g) (100 psig). At a feed temperature of 25 °C (77 F), the lubricant viscosity is $\mu = 2.81 \pm 0.01$ mPa-s ($40.7 \cdot 10^{-6}$ lbf.s/in²) and its density $\rho = 800 \pm 0.02$ kg/m³ (49.9 lb/ft³). The viscosity quoted is akin to that in an aircraft jet engine (~ 200 °C). Oil flows through a check valve and orifice into the middle plane of the film land ($z=0$). The journal has end grooves at $z = \pm \frac{1}{2} L$ for installation of end seals, either O-rings (OR), or piston rings (PR), or open to ambient (no end seals).

O-rings are very effective end seals since they offer a large flow resistance, practically null flow. In an OR-SFD configuration, see Fig. B2, the oil exits through one discharge orifice at $z = +\frac{1}{4} L$ that connects to a return line. A return pump

pushes the lubricant through a bubble eliminator and into a storage tank.

In the PR-SFD configuration, as shown in Fig. B3, the lubricant leaves the damper through the slits of the top and bottom piston rings. That is, as shown in Fig. 14 and Appendix A (videos), the lubricant ejects through the slit and simultaneously draws air into the squeeze film lands. The proper orientation of a PR when installed is crucial to ensure adequate sealing.

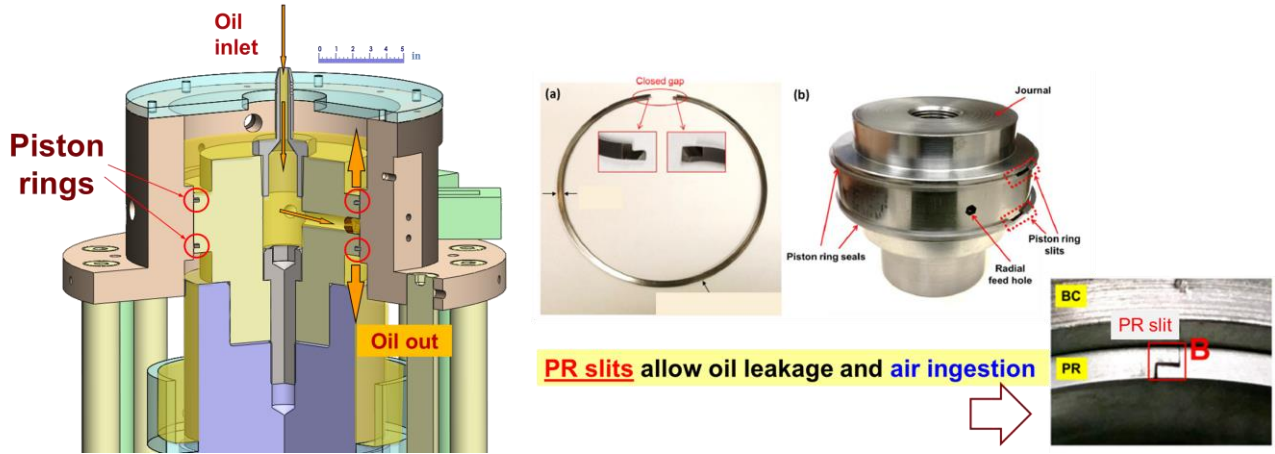


Fig. B3. PR-SFD: 3D cross section with lubricant flow path and views of journal and piston rings installed.

The experiments comprised single-frequency dynamic loads over a frequency range $\omega=10$ to 130 Hz, in increments of 10 Hz. The operation of the test rig is idealized as a two degree of freedom (DOF) mechanical system with the cartridge mass (M_{BC}) attached to the elastic support structure, the O-rings or PRs, and the squeeze film section. Fig. B4 showcases the idealized mechanical system and its fundamental parameters; namely, stiffness (K), damping (C), and inertia (M) force coefficients.

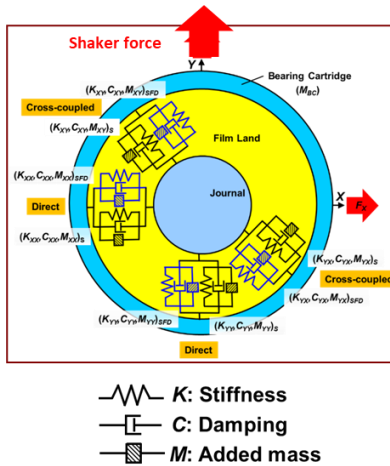


Fig. B4. Schematic view of SFD test rig as 2 DOF mechanical system.

Under lubricated conditions, the equation of motion in the frequency domain is

$$\mathbf{H}_{L(\omega)} \mathbf{Z}_{(\omega)} = \mathbf{F}_{(\omega)} - M_{BC} \mathbf{a}_{(\omega)} \quad (B1)$$

where $M_{BC}=15.6$ kg (34.4 lb) is the bearing cartridge mass, and $\mathbf{F}_{(\omega)}$, $\mathbf{Z}_{(\omega)}$ and $\mathbf{a}_{(\omega)}$ are complex vectors for the applied force, BC displacement relative to the journal, and BC absolute acceleration, respectively. Above, \mathbf{H}_L is a 2x2 matrix representing the lubricated system complex dynamic stiffness, and which includes the physical parameters from the structure, ORs or PRs, and the squeeze film. For the OR-SFD, let

$$\mathbf{H}_L = \mathbf{H}_{st+OR} + \mathbf{H}_{SFD} \quad (B2)$$

where

$$\mathbf{H}_{st+OR} = \mathbf{H}_{st} + \mathbf{H}_{OR} = \begin{cases} \mathbf{H}_{st} = [\mathbf{K}_{st} - \omega^2 \mathbf{M}_{st}] + i \omega \mathbf{C}_{st} \\ \mathbf{H}_{OR} = \mathbf{K}_{OR} + i [\omega \mathbf{C}_{OR} + \mathbf{K}_{\perp}] \end{cases} \quad (B3)$$

Above, the support structure has stiffness, damping and mass ($\mathbf{K}, \mathbf{C}, \mathbf{M}$)_{st}. The O-rings dynamic forced response is modeled with a viscous damping coefficient (\mathbf{C}_{OR}), a restoring stiffness (\mathbf{K}_{OR}), and a quadrature stiffness (\mathbf{K}_{\perp}).

Without the O-rings installed and no lubricant in the system, first measurements produce the support (\mathbf{H}_{st}), and curve fits over a frequency range deliver the physical parameters ($\mathbf{K}, \mathbf{C}, \mathbf{M}$)_{st}.

Next, the ORs are installed in the journal and still with a dry (no oil) structure, a new set of dynamic loads produces \mathbf{H}_{st+OR} , the parameters of the ORs plus the structure. Then, $\mathbf{H}_{OR} = [\mathbf{H}_{st+OR} - \mathbf{H}_{st}]$.

Lastly, lubricant is supplied into the damper at a set pressure (P_s), and a new round of dynamic load tests produces the complex dynamic stiffness \mathbf{H}_L of the lubricated system. The squeeze film parameters follow from $\mathbf{H}_{SFD} = \mathbf{H}_L - \mathbf{H}_{st+OR}$.

Curve fits over a certain frequency range produce the SFD stiffness, damping and added mass coefficients from

$$\mathbf{H}_{SFD} = [\mathbf{H}_L - \mathbf{H}_{st+OR}] \rightarrow [\mathbf{K}_{SFD} - \omega^2 \mathbf{M}_{SFD}] + i \omega \mathbf{C}_{SFD} \quad (B3)$$

The procedure for identifying the parameters of a SFD sealed with piston rings is identical.

As characteristic example, Fig. B5 displays the real and imaginary parts of the OR sealed SFD complex stiffnesses \mathbf{H}_{SFD} vs. excitation frequency for dynamic load tests with three whirl orbits of amplitude $r/c=0.05, 0.20$ and 0.45 . The symbols (squares and circles) denote the experimental data, whereas the dotted lines represent the curves built with the estimated parameters using the physical model $\text{Re}(\mathbf{H}_{SFD}) = (\mathbf{K}_{SFD} - \omega^2 \mathbf{M}_{SFD})$ and $\text{Im}(\mathbf{H}_{SFD}) = (\omega \mathbf{C}_{SFD})$. The estimation of the SFD stiffnesses spans a frequency range from $\omega=10$ to 40 Hz. Employing a larger frequency range (or $v_s > 24.5$ mm/s) would demand of a higher order fit model, likely devoid of physical significance.

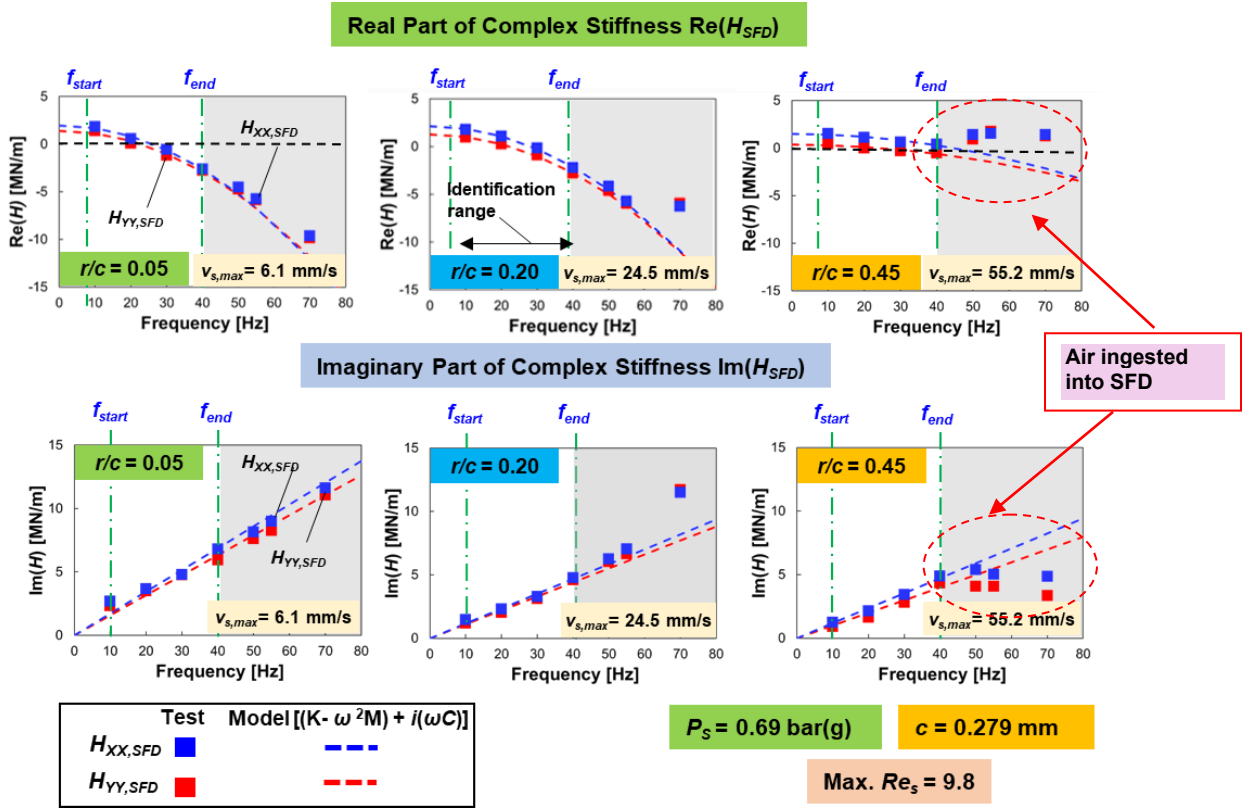


Fig. B5. OR-SFD: Real and imaginary parts of $(H_{XX}, H_{YY})_{SFD}$ vs. whirl frequency (ω) for three orbit radii. Clearance $c = 0.279$ mm. Supply pressure $P_s = 0.69$ bar(g). Identification of parameters ($\mathbf{K}, \mathbf{C}, \mathbf{M}$) in range $\omega = 10 - 40$ Hz. Reproduced from Ref. [2=19] (2024).

For $r = 0.05c$ and $0.20c$, $\text{Re}(\mathbf{H}_{SFD})$ decreases as frequency increases to show a significant added mass coefficient (\mathbf{M}_{SFD}).

However, for the larger orbit size ($r=0.45c$), $\text{Re}(\mathbf{H}_{SFD})$ grows as the whirl frequency increases (max. $v_s=55.25$ mm/s), and thus it produces a lesser virtual mass. For $v_s \geq 35$ mm/s, $\text{Re}(\mathbf{H}_{SFD}) \sim 0$; hence $M_{SFD} \sim 0$ or slightly negative.

Conversely, the bottom graphs in Fig. B5 show $\text{Im}(\mathbf{H}_{SFD})$ increases as $\omega \rightarrow 70$ Hz and $r < 0.45c$. The measurements evidence a dominant viscous damping coefficients, $\mathbf{C}_{SFD} \sim \text{Im}(\mathbf{H}_{SFD})/\omega$. Alas, as the whirl orbit amplitude grows to $r \sim 0.45c$, $\text{Im}(\mathbf{H}_{SFD})$ drops in magnitude for $v_s > 35$ mm/s, thus evidencing a rapid reduction in the squeeze film viscous damping effect. The drop in $\text{Im}(\mathbf{H}_{SFD})$ as the squeeze velocity increases (orbit size and frequency) is due to the pervasive presence of air ingestion in the squeeze film.

The force coefficients presented in the main body of this document are procured over a short frequency span, 10 Hz to 45 Hz. Incidentally, note the experimental cross-coupled force coefficients are (at least) one order smaller than the direct force coefficients and not shown for brevity.

REFERENCES (AS PER ASME STYLE, FINAL VERSION WILL IMPLEMENT TPS REFERENCING STYLE)

- [1] Vance, J., Zeidan, F., and Murphy, B., 2010, *Machinery Vibration and Rotordynamics*, Chapter 5, John Wiley and Sons, NY,
- [2] Childs, D.W., 2013, *Turbomachinery Rotordynamics with Case Studies*, Chapter 6, Minter Spring Pub., Wellborn, TX.
- [3] Barrett, L.E., Gunter, E. J., and Allaire, P.E., 1978, "Optimum Bearing and Support Damping for Unbalance Response and Stability of Rotating Equipment," *ASME J. Engineering for Power*, 100(1), pp. 89–94
- [4] Zeidan, F., San Andrés, L., and Vance, J., 1996, "Design and Application of Squeeze Film Dampers in Rotating Machinery," *Proc. of the 25th Turbomachinery Symposium*, Texas A&M University, September, pp. 169–188, <https://doi.org/10.21423/R1694R>
- [5] Kuzdal, M.J., and Hustak, J.F., 1996, "Squeeze Film Damper Bearing Experimental vs. Analytical Results for Various Damper Configurations," *Proc. of the 25th Turbomachinery Symposium*, Texas A&M University, September, pp. 57–70, <https://hdl.handle.net/1969.1/163442>
- [6] San Andrés, L., Jeung, S-H, Den, S., and Savela, G., 2016 "Squeeze Film Dampers: A Further Experimental Appraisal of their Dynamic Performance," 45th Turbomachinery Symposium, Texas A&M University, Sept 12-15, Houston, TX, <https://doi.org/10.21423/R1BC7T>
- [7] San Andrés, L., and Jeung, S.-H., 2016, "Orbit Model Force Coefficients for Fluid Film Bearings: A Step Beyond Linearization," *ASME J. Eng. Gas Turbines Power*, **138**(2):022502, <https://doi.org/10.1115/1.4031237>
- [8] San Andrés, L., and Koo, B., 2020, "Model and Experimental Verification of the Dynamic Forced Performance of a Tightly Sealed Squeeze Film Damper Supplied with a Bubbly Mixture," *ASME J. Eng. Gas Turbines Power*, 142(1): 011023, <https://doi.org/10.1115/1.4044994>
- [9] Koo, B., and San Andrés, L., 2023, "A Model and Experimental Validation for a Piston Rings - Squeeze Film Damper: a Step toward Quantifying Air Ingestion," *ASME J. Eng. Gas Turbines Power*, 145(4): 0410132, <https://doi.org/10.1115/1.4055712>
- [10] Lee, G.J., Kim, J., and Steen, T., 2017, Application of Computational Fluid Dynamics Simulation to Squeeze Film Damper Analysis," *ASME J. Eng. Gas Turbines Power*, **139**(10): 122501. <https://doi.org/10.1115/1.4036511>
- [11] Delgado, D., and San Andrés, L., 2010, "Identification of Squeeze Film Damper Force Coefficients from Multiple-Frequency, Non-Circular Journal Motions," *ASME J. Eng. Gas Turbines Power*, 132(4):042501, <https://doi.org/10.1115/1.3159374>
- [12] Reinhardt, F., and Lund, J. W., 1975, "The Influence of Fluid Inertia on the Dynamic Properties of Journal Bearings," 1975, *ASME J. Lubr. Technol.*, **97**(1), pp. 154-167.
- [13] Ramli, M.D., Roberts, J.B., and Ellis, J., 1987, "Determination of Squeeze-Film Dynamic Coefficients from Experimental Transient Data," *ASME J. Tribol.*, **109**(1), pp. 155-63.
- [14] Delgado, A., and San Andrés, L., 2010, "A Model for Improved Prediction of Force Coefficients in Grooved Squeeze Film Dampers and Grooved Oil Seal Rings," *ASME J. Tribol.*, **132**(3): 032202. <https://doi.org/10.1115/1.4001459>
- [15] Childs, D.W., Graviss, M., and Rodriguez, L.E., 2007, "The Influence of Groove Size on the Static and Rotordynamic Characteristics of Short, Laminar-Flow Annular Seals," *ASME J. Tribol.*, 129(2), 398-406.
- [16] Diaz, S., and San Andrés, L., 2001, "Air Entrainment Versus Lubricant Vaporization in Squeeze Film Dampers: an Experimental Assessment of their Fundamental Differences," *ASME J. Eng. Gas Turbines Power*, 123(4): 871-877, <https://doi.org/10.1115/1.1383258>
- [17] Gehannin, J., Arghir, M., and Bonneau, O., 2016, "A Volume of Fluid Method for Air Ingestion in Squeeze Film Dampers," *STLE Tribol. Trans.*, 59(2), pp. 208–218.

- [18] Gheller, E., Chatterton, S., Vania, A., and Pennacchi, P., 2022, “Squeeze Film Damper Modeling: a Comprehensive Approach,” *Machines*, 10(9), 781; <https://doi.org/10.3390/machines10090781>
- [19] Rodriguez, L., and San Andrés, L., 2024, “Dynamic Forced Response of an O-Rings Sealed Squeeze Film Damper Lubricated with a Low Supply Pressure and a Simple Method to Quantify Air Ingestion,” *ASME J. Eng. Gas Turbines Power*, 146(2): 021004, <https://doi.org/10.1115/1.4063320>
- [20] San Andrés, L., Koo, B.J., and Seung, J.-H., 2019, “Experimental Force Coefficients for Two Sealed Ends Squeeze Film Dampers (Piston Rings and O-rings): An Assessment of Their Similarities and Differences,” *ASME J. Eng. Gas Turbines Power*, 141(2), 02104, <https://doi.org/10.1115/1.4040902>
- [21] Zeidan, F., and Paquette, D.J., 1994, “Application of High Speed and High Performance Fluid Film Bearings in Rotating Machinery,” *Proc. 23rd Turbomachinery Symposium*, Texas A&M University, September, pp. 209-233, <https://hdl.handle.net/1969.1/163490>
- [22] Ertas, B., Cerny, V., Kim, J., and Polreich, V., 2015, “Stabilizing a 46 MW Multistage Utility Steam Turbine Using Integral Squeeze Film Bearing Support Dampers,” *ASME J. Eng. Gas Turb. Pwr.*, 137(5): 052506, <https://doi.org/10.1115/1.4028715>
- [23] Delgado, A., Cantanzaro, M., Mitaritonna, N., and Gerbet, M., 2011, “Identification of Force Coefficients in a 5-pad Tilting Pad Bearing with an Integral Squeeze Film Damper,” 10th PDF/prime Poitiers Workshop, Poitiers, France, October 6-7.
- [24] Agnew, J., and Childs, D.W., 2012, “Rotordynamic Characteristics of a Flexure Pivot Pad Bearing with an Active and Locked Integral Squeeze Film Damper,” *ASME Paper GT2012-68564*, <https://doi.org/10.1115/GT2012-68564>
- [25] Ertas, B., Delgado, A., and Moore, J., 2018, “Dynamic Characterization of an Integral Squeeze Film Bearing Support Damper for a Supercritical CO₂ Expander,” *ASME J. Eng. Gas Turb. Pwr.*, 140(5), p. 052501, <https://doi.org/10.1115/1.4038121>
- [26] Vannini, G., Giannelli, C., Matina, D., and Cangioli, F., 2024, “High Speed H₂ Centrifugal Compressor: a General Review of Journal Bearing Design and Experimental Validation,” *ASME paper GT2024-122482*, <https://doi.org/10.1115/GT2024-122482>
- [27] Lu, X., San Andrés, L., Koo, B., and Tran, S., 2021 “On the Effect of the Gap of End Seals on Force Coefficients of a Test Integral Squeeze Film Damper: Experiments and Predictions,” *ASME J. Eng. Gas Turb. Pwr.*, 143(1), p. 011014, <https://doi.org/10.1115/1.4048700>
- [28] Integral Squeeze Film Damper Design Guidelines, 2011, Waukesha Bearings, formerly KMC, Inc.

ACKNOWLEDGMENTS

Thanks to the Turbomachinery Research Consortium (TRC) at Texas A&M University, National Science Foundation (NSF), Pratt & Whitney Engines, General Electrical, Honeywell Aerospace, and other industries for their continued financial support and interest.

Dr. San Andrés is indebted to the dozens of graduate students (research assistants) and undergraduate students (student workers) whose work is hereby recognized. The tireless students, eager to learn and passionate of all things engineering, continue to make strides in their respective professional endeavors.